frontiers | Frontiers in Materials

TYPE Review
PUBLISHED 03 June 2024
DOI 10.3389/fmats.2024.1362744

MPX_3 van der Waals magnets under pressure (M = Mn, Ni, V, Fe, Co, Cd; X = S, Se)

Takahiro Matsuoka[1,2]*, Heung-Sik Kim[3]*, Subhasis Samanta[3], Janice L. Musfeldt[4]* and David G. Mandrus[1,5]*

[1]Department of Materials Science and Engineering, University of Tennessee, Knoxville, TN, United States, [2]National Institute of Physics, College of Science, University of the Philippines Diliman, Quezon, Philippines, [3]Department of Physics and Institute of Quantum Convergence Technology, Kangwon National University, Chuncheon, Republic of Korea, [4]Department of Chemistry, University of Tennessee, Knoxville, TN, United States, [5]Materials Science and Technology Division, Oak Ridge National Laboratory, Oak Ridge, TN, United States

OPEN ACCESS

EDITED BY
Leszek A. Majewski,
The University of Manchester,
United Kingdom

REVIEWED BY
Souvik Banerjee,
Intel, United States
Shuai Dong,
Southeast University, China

*CORRESPONDENCE
Takahiro Matsuoka,
✉ tmatsuoka@up.edu.ph
Heung-Sik Kim,
✉ heungsikim@kangwon.ac.kr
Janice L. Musfeldt,
✉ musfeldt@utk.edu
David G. Mandrus,
✉ dmandrus@utk.edu

RECEIVED 28 December 2023
ACCEPTED 23 February 2024
PUBLISHED 03 June 2024

CITATION
Matsuoka T, Kim H-S, Samanta S, Musfeldt JL and Mandrus DG (2024), MPX_3 van der Waals magnets under pressure (M = Mn, Ni, V, Fe, Co, Cd; X = S, Se).
Front. Mater. 11:1362744.
doi: 10.3389/fmats.2024.1362744

van der Waals antiferromagnets with chemical formula MPX_3 (M = V, Mn, Fe, Co, Ni, Cd; X = S, Se) are superb platforms for exploring the fundamental properties of complex chalcogenides, revealing their structure-property relations and unraveling the physics of confinement. Pressure is extremely effective as an external stimulus, able to tune properties and drive new states of matter. In this review, we summarize experimental and theoretical progress to date with special emphasis on the structural, magnetic, and optical properties of the MPX_3 family of materials. Under compression, these compounds host inter-layer sliding and insulator-to-metal transitions accompanied by dramatic volume reduction and spin state collapse, piezochromism, possible polar metal and orbital Mott phases, as well as superconductivity. Some responses are already providing the basis for spintronic, magneto-optic, and thermoelectric devices. We propose that strain may drive similar functionality in these materials.

KEYWORDS

van der Waals solids, complex chalcogenides, external stimuli, antiferromagnetic ordering, insulator-metal transition, structural transition, magnetic transition, pressure

1 Introduction

Transition metal phosphorous trichalcogenides, MPX_3, where M represents a transition metal ion and X is either S or Se, are a family of semiconducting van der Waals magnets that were originally discovered in 1894 (Friedel, 1894) but were not studied intensively until the 1970s (Klingen et al., 1973). Originally, interest in these materials was sparked by their low dimensional magnetic properties (Le Flem et al., 1982) and ability to form intercalation compounds (Jophnson and Jacobson, 1982), although more recently these materials have attracted attention as single-layer magnets (Burch et al., 2018) and as highly tunable systems that undergo bandwidth-controlled Mott transitions under pressure (Kim et al., 2019).

MPX_3 materials typically crystallize in two space groups, $C2/m$ (No. 12) for the sulfur analogs and $R\overline{3}$ (No. 148) for the selenium-containing compounds. In both cases, the M ions form a honeycomb net, and at the center of each hexagon there is a P-P dimer that extends perpendicular to the net. S or Se anions terminate each MPX_3 layer on both sides, and there is a van der Waals gap between the layers, leading to small cleavage energies and easy exfoliability. Single layers of the MPS_3 and $MPSe_3$ materials can also be viewed as a honeycomb net of M^{2+} ions coordinated by distorted octahedra of S/Se anions, and P-P dimers centering the hexagons and forming a $[P_2S_6]^{4-}$ anionic sublattice (Figure 1). To emphasize the importance of the P-P dimers, the chemical formula of MPX_3 materials is sometimes written as $M_2P_2X_6$, but this is incorrect nomenclature as the chemical formula is not supposed to reflect structural features (Hiroi, 2008). These structural motifs lead to three different types of chemical bonding: ionic, covalent, and van der Waals - which makes understanding the electronic structure of this family of materials quite challenging (Dedkov et al., 2023).

In general, MPS_3 materials with M = V, Mn, Fe, Co, and Ni are reported to be antiferromagnetic Mott insulators with variable semiconducting energy gaps and magnetic structures. $CdPS_3$, in contrast, has a filled d shell and is semiconducting and nonmagnetic. The Mottness and magnetism of MPS_3 compounds originates from their partially-filled d-orbital shells; this, in addition to the presence of a van der Waals gap, suggests that the MPS_3 series is an excellent platform for the study of two-dimensional correlated electron phenomena and magnetism (Figure 1).

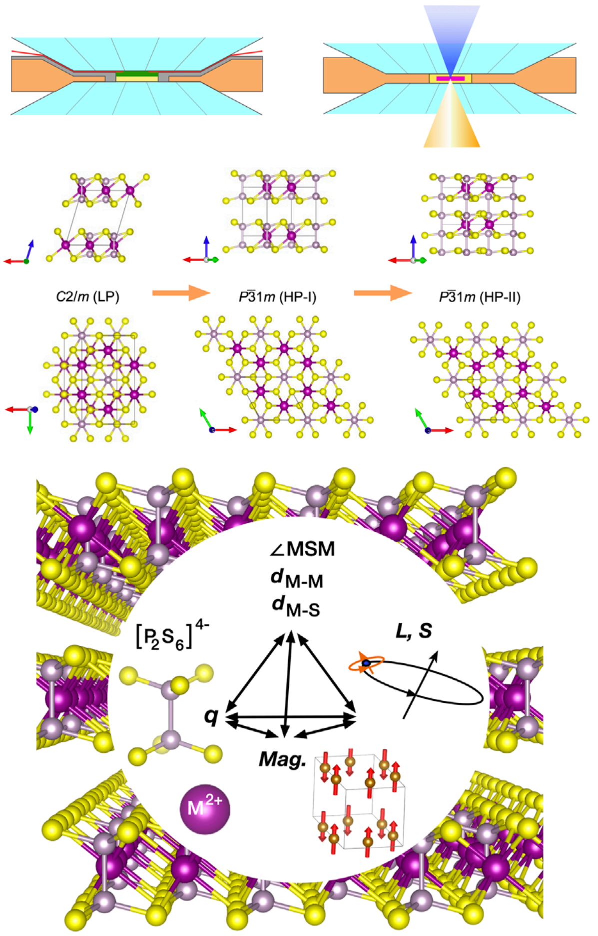

FIGURE 1
(Top) Schematic diagrams of diamond anvil cells (DAC) applying hydrostatic (left) and non-hydrostatic (right) pressure to MPX_3 compounds. (Middle) An example of pressure-induced structural transition involving layer sliding and phosphorous chain formation in MPX_3. (Bottom) An Illustration of structural (metal-metal distance d_{M-M}, metal-sulfur distance d_{M-S}, and bond angle $\angle MSM$), orbital (L), spin (S), charge (q)), and magnetic (*Mag.*) degrees of freedom, which together interact to give rise to novel pressure-induced physical properties of MPX_3.

Tuning the physical properties of these compounds is a highly contemporary research subject, allowing for the exploration of new states of matter and functionalities. Toward this end, researchers are using chemical substitution, doping and intercalation, as well as various external perturbations such as electric field, light, strong magnetic fields, and strain (Wang et al., 2018a; Pei et al., 2022). For instance, chemical substitution on the M and X sites provides the control of d-orbital filling and bandwidth, respectively, which are both important parameters to control Mottness, magnetism, and spin-orbital-lattice coupling (Lu et al., 2022; Peng et al., 2023). Even better, many MPS_3 compounds have both X = S and Se limits as stable systems, which allows continuous tuning of lattice parameters and bandwidth via synthesizing MPS_xSe_{3-x} samples (Basnet et al., 2022b). Even differences in X-site chemistry sometimes gives rise to interesting contrasts; for example, the presence and absence of superconductivity in pressurized $FePSe_3$ and $FePS_3$, respectively. At the same time, doping and intercalation control carrier concentration and impart new properties (Basnet et al., 2022a; Tezze et al., 2022).

Among these external stimuli, pressure is a highly effective tool for tuning the physical properties of MPX_3 materials. The interlayer van der Waals (vdW) interaction is weak; thus, the interlayer spacing can be effectively modulated by pressure. As the layers are forced closer together, layers slide with respect to each other, changing their relative orientation. Furthermore, pressure modifies the c/a ratio, reflecting the more compressible interlayer distance than the ab plane. Bond lengths and angles within the chalcogenide layers are also modified under compression (Figure 1). With the collapse of the van der Waals gap under pressure, interlayer orbital overlap increases, and the materials become more three-dimensional with enhanced bandwidth. With varying d-orbital occupancies and the resulting different orbital degrees of freedom (i.e., t_{2g} vs. e_g), pressure can induce drastically different responses of lattice structure, as well as electronic and magnetic properties, depending on the chemistry of the metal center and chalcogen anion.

In addition to bandwidth and dimensionality tuning, the sliding of adjacent layers and change of stacking order can create contrasting responses in electronic and magnetic properties, as recently suggested in 1T-TaS_2 with the "star of David" charge density wave formation. In MPX_3, this effect appears prominently since even hydrostatic pressure can create shear strain in the monoclinic structure of many of them (Butler et al., 2020). As we will see below, the presence of this layer-sliding in the MPS_3 series under pressure (in $V_{0.9}PS_3$, $MnPS_3$, $FePS_3$, $CoPS_3$, and $NiPS_3$) creates complicated yet rich structural, electronic, and magnetic behaviors. For example, it has been reported that the layer sliding in $MnPS_3$ expedites the pressure-induced Mott transition (Harms et al., 2020). At this point it is uncertain why systems show different layer-sliding responses under compression, still it is clear that pressure is a valuable tool in unlocking tremendously rich physical characteristics hidden within the MPX_3 series.

Over the past few years the evolution of the structural, magnetic, and electronic properties of MPX_3 compounds under compression have been extensively studied. Given the rapid progress in this field, the time is ripe for a short review. In the sections below, we first discuss the M = Mn, Fe, and Ni, which have been the topics of the most number of studies. We then discuss $V_{0.9}PS_3$ and $CoPS_3$, which have been much less studied. Lastly, we cover the non-magnetic compounds, $CdPS_3$ and $CdPSe_3$, and the structure-property relations that can be unraveled in these systems.

In addressing ongoing research topics in each system, discussions involving the following themes occur in most of the compounds: strong electron correlations from the partially-filled d-orbital shells, pressure-induced Mott insulator-to-metal transitions, the role of p-d hybridization in ground-state and optical properties via the comparison between MPS_3 and $MPSe_3$ systems, and the role of layer-sliding and the changes in of P-P bonding at the Mott metallization transition. These issues are discussed at appropriate points in the manuscript.

Pressure is an effective tool for tuning the properties of complex chalcogenides, but the following considerations should be kept in mind when interpreting experimental data. Below 6 or 7 GPa, pressure in the diamond anvil cell is reliably hydrostatic, although tests should be performed to confirm this expectation. Above 6 or 7 GPa, it's very challenging to assure perfectly hydrostatic conditions. Even in a well-tested and characterized system, there may be deviations on the order of 1% or more—especially at low temperatures. Non-hydrostatic conditions can impact the properties - for instance, broadening a spectroscopic response. These signatures are most easily monitored by ruby fluorescence and are discussed in a number of references including (Musfeldt et al., 2023).

2 Properties of MPX_3 materials under pressure

2.1 $MnPS_3$ and $MnPSe_3$

$MnPS_3$ is the prototype in this family of materials and is therefore extensively investigated. This system crystallizes in a monoclinic $C2/m$ structure whereas $MnPSe_3$ displays a trigonal $R\overline{3}$ arrangement. The P–P dimer is an important structural building block as is the $P_2S_6^{4-}$ cluster. These elements are crucial in defining the thickness of the chalcogen layer. Table 1 summarizes the layer thickness and van der Waals gap for $MnPS_3$ and $MnPSe_3$ and compares them to other members of this series. The $C2/m$ vs. $R\overline{3}$ structural difference between sulfur and selenium analogs plays out in other members of the MPX_3 family of materials as well (Figure 2 and Tables 2, 3).

Early neutron diffraction studies of $MnPS_3$ uncovered collinear Néel-type AFM order at T_N = 78 K (Le Flem et al., 1982; Kurosawa et al., 1983b; Joy and Vasudevan, 1992; Wildes et al., 1994), although there were discrepancies as to the direction of the magnetic propagation vector. A recent study revisited this problem using single crystal neutron diffraction and polarimetry (Ressouche et al., 2010). This work revealed a propagation vector $\boldsymbol{k}$ = [000] as well as magnetoelectric coupling and ferrotoroidicity (Ressouche et al., 2010). By comparison, T_N = 74 K for $MnPSe_3$ (Wiedenmann et al., 1981; Le Flem et al., 1982). A similar reduction of the transition temperature is observed for $FePX_3$ when the X is modified from sulfur to selenium. Neutron scattering of $MnPSe_3$ reveals an identical propagation vector ($\boldsymbol{k}$ = [000]) (Wiedenmann et al., 1981; Bhutani et al., 2020). Photoemission and x-ray absorption spectroscopy confirms a high spin Mn^{2+} configuration in $MnPSe_3$ (Fujii et al., 2022). Each Mn center is antiferromagnetically coupled to its three nearest neighbors (Kurosawa et al., 1983a). One surprising finding is the strong magnetic interaction between third nearest neighbors. The spin wave excitations have also been studied by Raman and neutron scattering in these materials. Major findings include: hybridization of the two-magnon excitation with phonons (which impacts the spin wave decoherence pathway) and absence of nonreciprocity in zone boundary magnons (which provides experimental limits that can be tested against theoretical predictions) (Sun et al., 2019; Vaclavkova et al., 2020; Mai et al., 2021; Wildes et al., 2021).

Several different but complementary efforts were required to unravel the sequence of events that takes place under pressure. In the first experimental work, Wang et al. uncovered a simultaneous spin-state crossover and metal-insulator transition in both $MnPS_3$ and $MnPSe_3$ (Figure 3) as well as zigzag chain formation of the Mn atoms in the metallic phase (Wang et al., 2016). The critical pressures (P_c's) for these processes were reported to be 30 and 25 GPa for $MnPS_3$ and $MnPSe_3$, respectively. First-principles electronic structure calculations using DFT + U and DFT + DMFT techniques reproduced the insulator-to-metal transition with simultaneous spin-state transition but with a Mn-Mn dimerization at 64 GPa (Kim et al., 2019), although it was hinted that some structural components might be missing. This early experimental and theoretical work did not consider layer sliding, which turns out to modify the picture in important ways.

TABLE 1 Inter-layer thicknesses distances and van der Waals (vdW) gaps of MPS_3 and $MPSe_3$. Data are from (Ouvrard et al., 1985b; Ouvrard et al., 1985a; Wiedenmann et al., 1981).

	$V_{0.78}PS_3$	$MnPS_3$	$FePS_3$	$CoPS_3$	$NiPS_3$	$CdPS_3$	$MnPSe_3$	$FePSe_3$
layer thickness (Å)	6.363	6.487	6.423	6.361	6.343	6.546	6.673	6.604
vdW gap (Å)	3.227	3.247	3.250	3.243	3.258	3.218	3.275	3.174
(layer thickness)/(vdW gap)	0.507	0.500	0.506	0.510	0.514	0.492	0.491	0.481

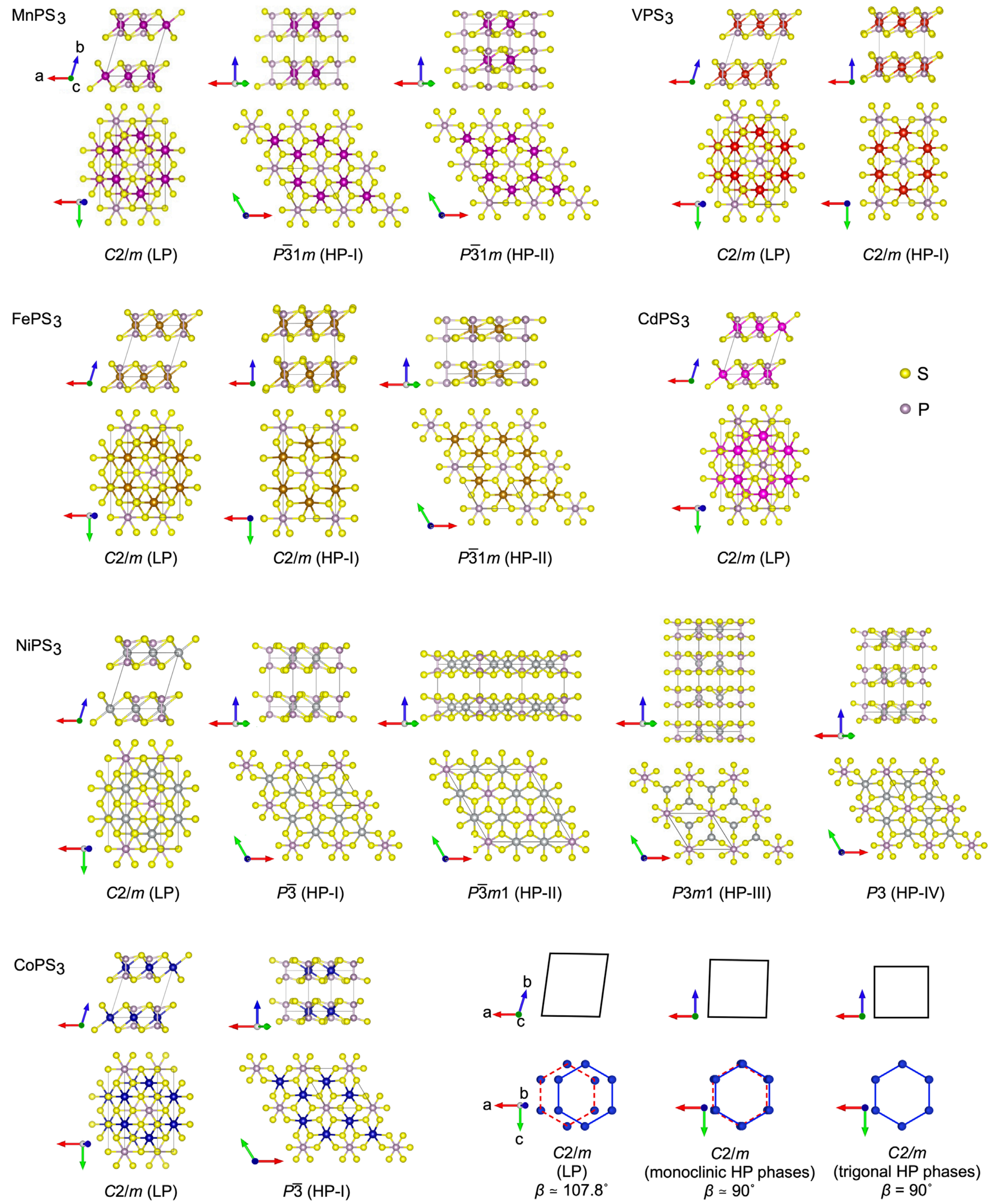

FIGURE 2
Crystal structures of MPS_3 (M = V, Mn, Fe, Ni, Co, Cd) family of materials in the low-pressure (LP) and high-pressure (HP) phases visualized using VESTA3 (Momma and Izumi, 2011) based upon reported experimental and theoretical results (Ouvrard et al., 1985a; Haines et al., 2018; Coak et al., 2019; Harms et al., 2020; Harms et al., 2022a; Matsuoka et al., 2023). The bottom right shows layer sliding in *C*2/*m* symmetry with decreasing monoclinic angle β under pressure. When $\beta = 90°$, the honeycomb pattern of metal ions overlaps between adjacent layers, and the system transforms to a trigonal high pressure phase.

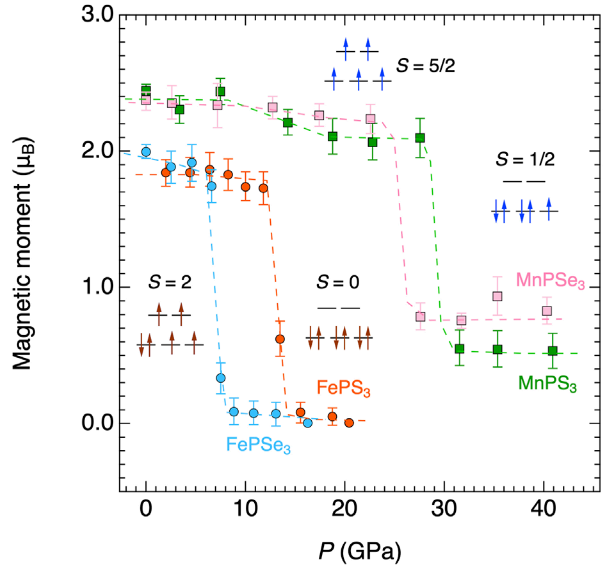

FIGURE 3
Magnetic moment and spin state as a function of pressure for $MnPS_3$, $MnPSe_3$, $FePS_3$, and $FePSe_3$ relative to properties at ambient conditions. Data taken from (Wang et al., 2016; Wang Y. et al., 2018).

In a significant conceptual advance, Coak et al. discovered an intermediate pressure transition in the series of MPS_3 (M = $V_{0.9}$, Mn, Fe, Ni) materials (Coak et al., 2020). This transition involves coherent layer sliding to create an alignment of P–P dimers along the layer-normal direction. This insight enabled a number of subsequent advancements. For instance, infrared, Raman scattering, and optical measurements as a function of pressure combined with first-principles calculations reveal that $MnPS_3$ undergoes a $C2/m$ (LP) → $P\bar{3}1m$ (HP-I, insulating, around 10 GPa) → $C2/m$ (HP-II, metallic, around 30 GPa) with a layer-sliding between the LP and HP-I phases, similar to observed in $FePS_3$ (Figure 2 and Table 2). The HP-I → HP-II transition accompanies spin-state transition, collapse of MnS_6 volume, and a reduction of interlayer distance with an layer-normal P-chain formation, (Figures 2–4). The trigonal (HP-I)-to-monoclinic (HP-II) symmetry lowering transition is thought to originate from the low-spin d^5 orbital nature of the Mn^{2+} ions, contrary to the case of $FePS_3$ with the same layer sliding but with $C2/m$ (LP) → $C2/m$ (HP-I, insulating after the layer sliding) → $P\bar{3}1m$ (HP-II, metallic) transitions.

We note in passing that theory tends to over-estimate the band gap and pressure of the insulator-to-metal transition in these materials (Grasso et al., 1991; Harms et al., 2020; Yan et al., 2023). Gap estimation is a well-known challenge for first-principles density functional theory-based approaches, and weak interactions with shallow potentials are notoriously difficult to calculate with accuracy. Nevertheless, these techniques nicely reveal the semiconducting behavior of the aligned phosphorous dimer phase and the metallic character of the aligned phosphorous chain phase (Figure 5A).

From the optical properties point of view, $MnPS_3$ is a semiconductor with a 2.7 eV band gap. It hosts spin-charge coupling across the magnetic ordering transition and a set of crystal field excitations that have been widely investigated (Boerio-Goates et al., 1981; Grasso et al., 1991; Harms et al., 2020; Yan et al., 2023; Park et al., 2024). There is strong p-d hybridization which activates the d-to-d on-site excitations of the Mn^{2+} centers. There is also a broad near infrared emission band assigned as $^4T_1 \rightarrow {}^6A_1$

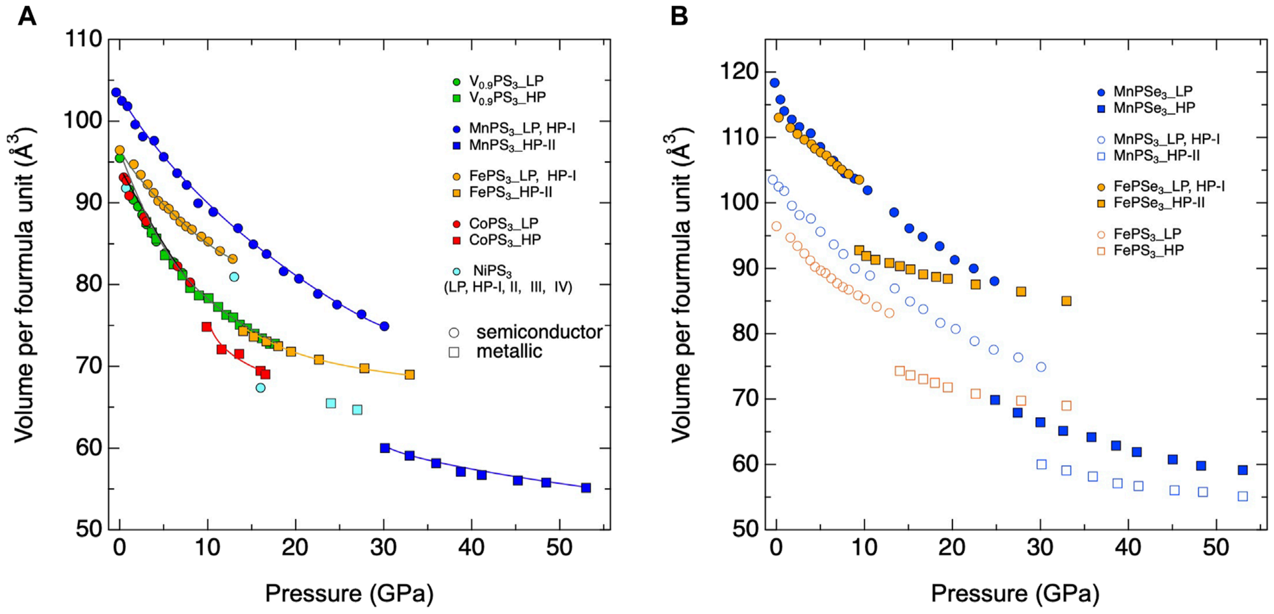

FIGURE 4
Volume per formula unit as a function of pressure. **(A)** MPS_3 (M = V, Mn, Fe, Co, Ni). **(B)** $MnPS_3$ and $FePS_3$ with $MnPSe_3$ and $FePSe_3$ for comparison. The circles denote the low (or ambient) pressure phase, which is semiconducting, including the HP-I phases for $MnPS_3$ and $FePS_3$. The squares indicate high pressure metallic phases. The solid lines guide the eye.

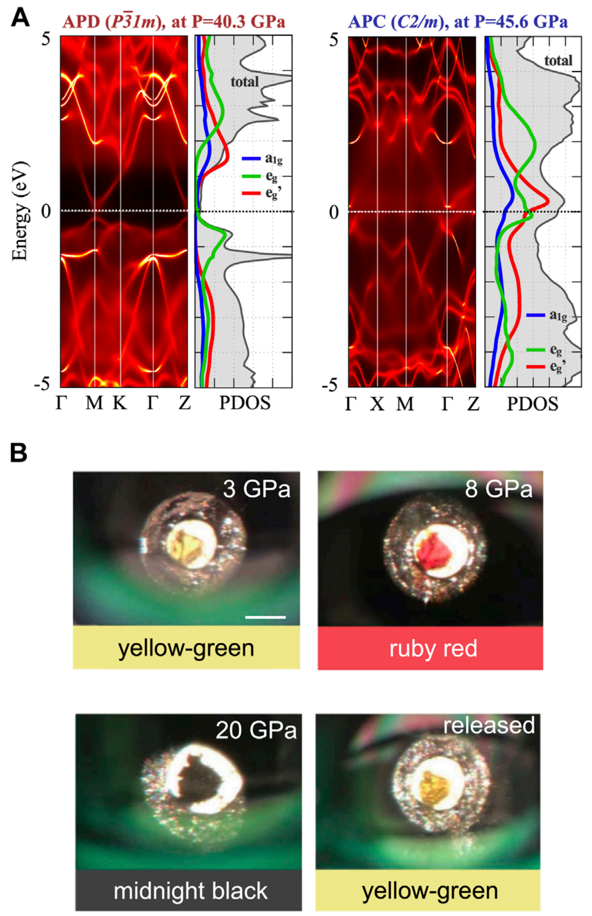

FIGURE 5
$MnPS_3$ under pressure puncture. **(A)** Spectral functions from DFT + DMFT calculations showing the k-resolved and orbital-projected spectral functions calculated with the aligned phosporous dimer (APD) and aligned phosphorous chain (APC), respectively (Harms et al., 2020). **(B)** Photographs of piezochromic $MnPS_3$ inside the diamond anvil cell at several characteristic pressures and also after release at room temperature. The scale bar (left panel) is 200 μm. (Harms et al., 2020).

with a half life of approximately 50 μs at 77 K (Boerio-Goates et al., 1981). The ratio of the crystal field splitting to the Racah parameter ($10Dq/B$) is unusually large and may explain the strongly red-shifted light emission in this system. That the band gap of $MnPS_3$ decreases systematically under pressure suggests that this system hosts piezochromism (Harms et al., 2020). It turns out that $MnPS_3$ is green at ambient conditions, and as shown in Figure 5B, it is yellowish-green at 3 GPa, bright red at 8 GPa, and black by 20 GPa. The latter occurs because the band gap shifts out of the visible wavelength range, moving systematically toward closure at a rate of approximately −50 meV/GPa. This effect is quenched by the appearance of the insulator–metal transition. This high level of linear responsivity under pressure is unusual, and piezochromism of this type has applications in pressure sensing, actuation, as well as artificial skin. At this time, it is not known whether strain can drive similar effects in the bulk material, although in few- and single-sheet $MnPS_3$ there is a $C2/m$ to $P\bar{3}1m$ transition that may involve surface strain effects (Neal et al., 2019; Neal et al., 2020) and biaxial strain is predicted to impact the magnetic ground state in $MnPSe_3$ monolayers (Pei et al., 2018).

Thermal properties of these materials are also of interest from a fundamental point of view and for heat management purposes in a device. Kargar et al. find in- and out-of-plane thermal conductivities of 6.3 ± 1.7 and 1.1 ± 0.2 W/m·K, respectively (Kargar et al., 2019). These values are higher than what is found in the Fe analog.

2.2 $FePS_3$ and $FePSe_3$

$FePS_3$ and $FePSe_3$ are layered antiferromagnets with T_N around 120 K (Le Flem et al., 1982; Joy and Vasudevan, 1992). $FePS_3$ has gained significant interest recently for its Ising-like antiferromagnetic ordering in the single-layer limit (Lee et al., 2016). The d^6 configuration of the Fe^{2+} charge status shows a high-spin configuration $S = 2$ with the partially-filled t_{2g} complex, implying anisotropic nature of magnetism as revealed by experimental and theoretical observations (Nauman et al., 2021; Zhang et al., 2021). In the presence of external pressure, like Mn-based siblings, spin-state transition and the resulting complex electronic and structural responses are expected in $FePS_3$ and isostructural $FePSe_3$. Accordingly, the responses of magnetic, electronic, and structural properties of $FePS_3$ and $FePSe_3$ have been actively investigated.

Recent x-ray, neutron scattering, and optical spectroscopy studies on the effect of hydrostatic pressure on $FePS_3$ reveal a sequence of structural phase transitions, (Haines et al., 2018; Coak et al., 2021; Harms et al., 2022b) analogous to $MnPS_3$ and $V_{1-x}PS_3$ (Coak et al., 2019; Harms et al., 2020); a gradual layer-sliding crossover from the monoclinic LP ($C2/m$ space group) to the pseudo-hexagonal intermediate phase (HP-I, $C2/m$) around 2–5 GPa, and the following $C2/m \rightarrow P\bar{3}1m$ (HP-II) transition accompanied by the insulator-to-metal transition at 14 GPa (see Figure 2), (Coak et al., 2021). The LP and HP-I phases of $FePS_3$ have been reported to be insulating and antiferromagnetic with a Néel-type order. Figures 6A, B show the magnetic configurations of the LP and HP-I phases from neutron data, respectively (Coak et al., 2021). Figure 6C describes the evolution of the T_N as a function of pressure (Wang et al., 2018b; Haines et al., 2018; Coak et al., 2021). The gradual enhancement of the T_N can be attributed to the increased kinetic energy scale due to the closer Fe-Fe distances and the resulting enhanced magnetic exchange interactions.

The second transition (HP-I → HP-II) accompanies the breaking of the P-P dimer structure and the formation of interlayer P-chain perpendicular to the Fe layers, in addition to a sudden collapse of the interlayer distance and volume, (Haines et al., 2018) similar to the case of $MnPS_3$. Harms et al. (2020) note that these observations are consistent with separate first-principles electronic structure calculation results, (Zheng et al., 2019; Deng et al., 2023) where the origin of the coexistence of the LP and HP-I phases around 2–5 GPa is suggested to be the result of the shear-induced energy barrier between the LP and HP-I phases (see Figure 7A), (Deng et al., 2023).

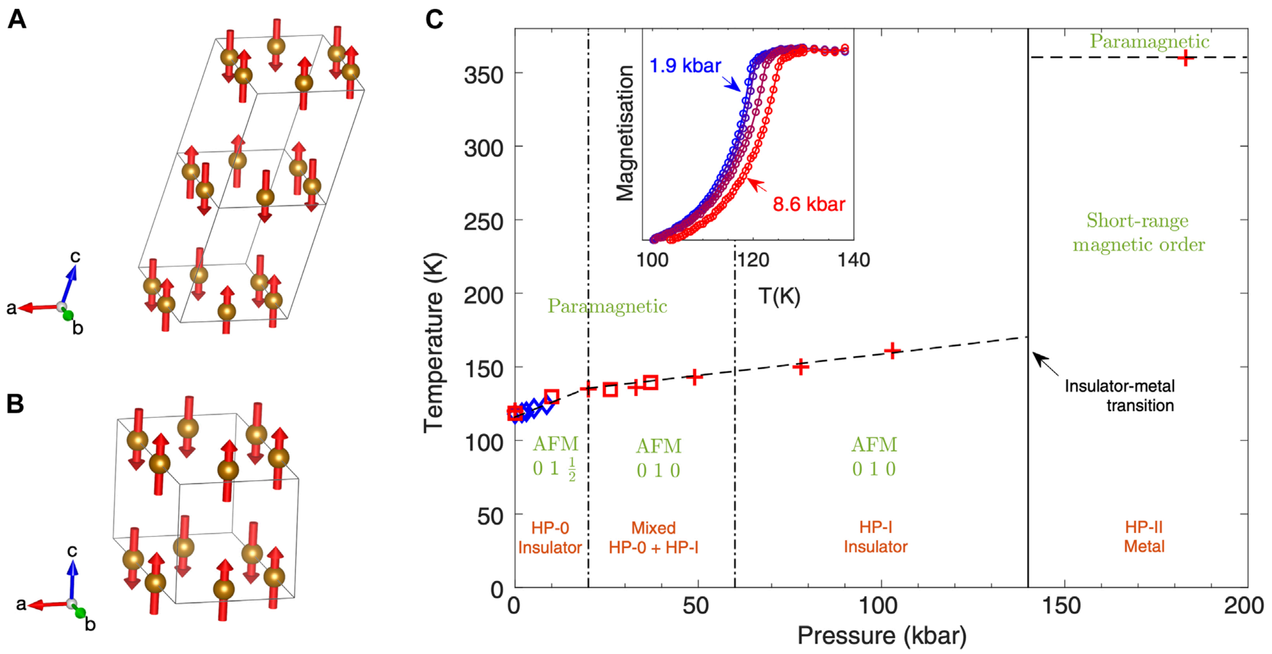

FIGURE 6
Crystal and magnetic structures of the low-pressure (HP-0) and the first high-pressure (HP-I) phases of $FePS_3$. **(A)** The magnetic cell of $FePS_3$ with the ***k*** = [0 1 1/2] propagation vector - overall antiferromagnentic order, consisting of a zig-zag chain antiferromagnetically coupled to their neighbors along *a*-axis and between the planes (Lançon et al., 2016). **(B)** The magnetic unit cell with ***k*** = [0 1 0] propagation vector, where the planes are ferromagnetically aligned (Coak et al., 2021). **(C)** Pressure-temperature phase diagram of $FePS_3$ from magnetization measurements and neutron scattering experiments. Blue circles, red crosses (and squares) are from magnetization measurements and integration of neutron spectra, respectively. Dashed lines are fits to the data points, and vertical lines mark structural transitions. Inset shows normalized magnetization *versus* temperature with increasing pressure. The plot is from (Coak et al., 2021).

From both experimental and theoretical studies, the Mott-insulating antiferromagnetic phase is reported to remain robust in the LP and HP-I phases, reflecting the quasi-two-dimensional nature (Haines et al., 2018; Zheng et al., 2019). With the formation of the interlayer P-chain in the HP-II phase this two-dimensional character breaks down, and so does the insulating behavior. The sudden collapse of the interlayer distance and cell volume at the HP-I → II transition implies a spin-state transition (see Figure 4). Indeed, an early study on pressurized phases of $FePS_3$ and $FePSe_3$ reported collapses of magnetic moments and transitions to low-spin phases around 13 and 8 GPa, respectively, Wang et al. (2018b) and additionally, the DFT study of Zheng et al. (2019) also reports the spin-state transition from the high-spin $S = 2$ to the low-spin $S = 0$ configuration of the Fe ions at the HP-I → II transition. Interestingly, on the other hand, a high-pressure neutron diffraction data by Coak et al. (2021) suggests the presence of short-range magnetic order in the HP-II phase, persisting even up to room temperature (see Figure 6C, 7B). From a detailed electronic structure calculation study, Deng et al. (2023) argues that this puzzling behavior may be explained by the potential coexistence of two metastable metallic states; the high-spin one with the intralayer P_2 dimer structure remains intact comparing the short-range order (2D-like), while the P_2 dimer breaks to form the out-of-plane P chain structure (3D-like) in the other low-spin state. A separate dynamical mean-field theory study on $FePS_3$ also suggests the coexistence of the two structural phases, each one hosting the normal Fermi liquid-like character (with the interlayer P-chain) and the incoherent “Hund’s metal” character (with the intralayer P-dimer) in the high-pressure regime, where the Hund’s metal phase keeps the local moments intact and induces bad-metallic behavior due to magnetic fluctuations (Kim et al., 2022).

It is interesting to note that, in Kim et al., (2022), the Hund’s metal phase with the orbital-selective correlation effects occurs only with a non-hydrostatic pressure, especially when the pressure perpendicular to the Fe layers are stronger than the in-plane counterparts. This originates from the direction-selective orbital effect under pressure, where the t_{2g} orbitals of Fe ions becomes more susceptible to the out-of-plane stress compared to e_g. This implies a subtle role of anisotropy and inhomogeneity in pressure, which may often occur in high-pressure experimental situations depending on the choices of pressure-transmitting medium (Matsuoka et al., 2021).

Lastly we comment on $FePSe_3$. This system shares a crystal structure and magnetic ground state with $FePS_3$, (Wiedenmann et al., 1981; Le Flem et al., 1982) and expected from theoretical calculations to show many common properties, such as layer-sliding transition to HP-I, volume collapse at the HP-I → II transition accompanying the simultaneous spin-state and insulator-metal transitions (Zheng et al., 2019). Experimentally the second

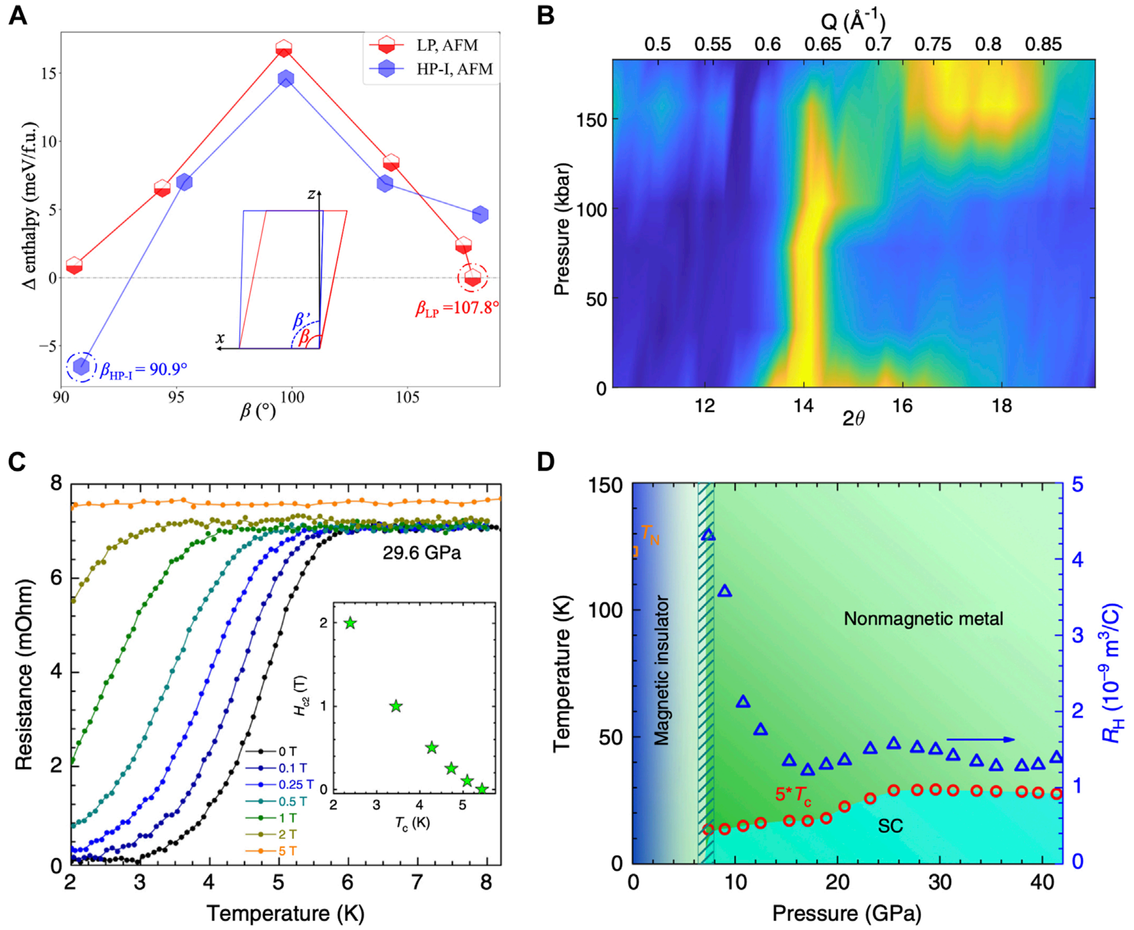

FIGURE 7
High-pressure electronic states of $FePS_3$ and superconducting $FePSe_3$ **(A)** Enthalpy difference from DFT calculations as a function of the monoclinic β angle in the $C2/m$ structure for the ambient (LP) and HP-I AFM phases of $FePS_3$ at 1.0 GPa. Panel from Deng et al. (2023). **(B)** Heat map of magnetic peaks at 80 K in $FePS_3$, showing the presence of magnetic signals in the HP-II ($P > 15$ GPa) phase. Panel from Coak et al. (2021). **(C)** The temperature dependence of the electrical resistance of $FePSe_3$ at 29.6 GPa under magnetic fields of 0, 0.1, 0.25, 0.5, 1, 2, and 5 T. Inset shows the field dependence of T_c for $FePSe_3$ at 29.6 GPa. **(D)** Temperature−pressure phase diagram of $FePSe_3$. Solid circles: the pressure dependence of the onset superconducting transition temperatures ($5 * T_c$), blue triangles: the pressure dependence of Hall coefficient, T_N denoting the Néel temperature. Panel **(C)** and **(D)** from (Wang Y. et al., 2018).

transition is observed to occur at a lower pressure of around 8 GPa than that of $FePS_3$, which can be attributed to the larger hybridization effects from Se ions (Wang et al., 2018b). Unlike $FePS_3$, superconductivity of unknown origin has been reported in the HP-II metallic phase of $FePSe_3$ below 2.5K (see Figures 7C, D), (Wang et al., 2018b). Structural refinement in the same study suggests the formation of the zigzag chains within the Fe honeycomb layer in the HP-II phase of $FePSe_3$, hinting the presence of orbital physics from high-spin configuration at Fe ions and potential unconventional superconductivity.

2.3 $NiPS_3$ and $NiPSe_3$

$NiPS_3$ and the Se analog provide another exciting platform for exploring new states of matter under external stimuli and developing different types of structure-property relationships. The magnetic ordering temperatures are T_N = 155 and 206 K, respectively (Le Flem et al., 1982; Joy and Vasudevan, 1992; Chandrasekharan and Vasudevan, 1994), so we see that in this case, heavier anions act to raise the Neél temperature. In the low temperature phase of $NiPS_3$, the magnetic propagation vector $\boldsymbol{k} = [010]$. Analysis of the integrated intensity of the (010) magnetic Bragg peak as a function of temperature reveals a critical exponent for the magnetization $2\beta = 0.30$ away from the transition temperature, consistent with a two-dimensional universality class, and 0.30 near T_N, suggesting the importance of three-dimensional interactions in this regime (Wildes et al., 2015). There are a number of low energy excitations in this system from which competing exchange interactions can be extracted (Mehlawat et al., 2022; Wildes et al., 2023), and active pumping of orbital resonances can also manipulate magnetic order in this quasi-two-dimensional van der Waals antiferromagnet (Afanasiev et al., 2021). Solid solutions in the form of $Ni_{1-x}Mn_xPS_3$ ($0 \leq x \leq 1$) can also tune the spin flop transition from approximately 7 to 2 T due to modulation of the magnetic anisotropy (Basnet et al., 2021). Intercalation is also

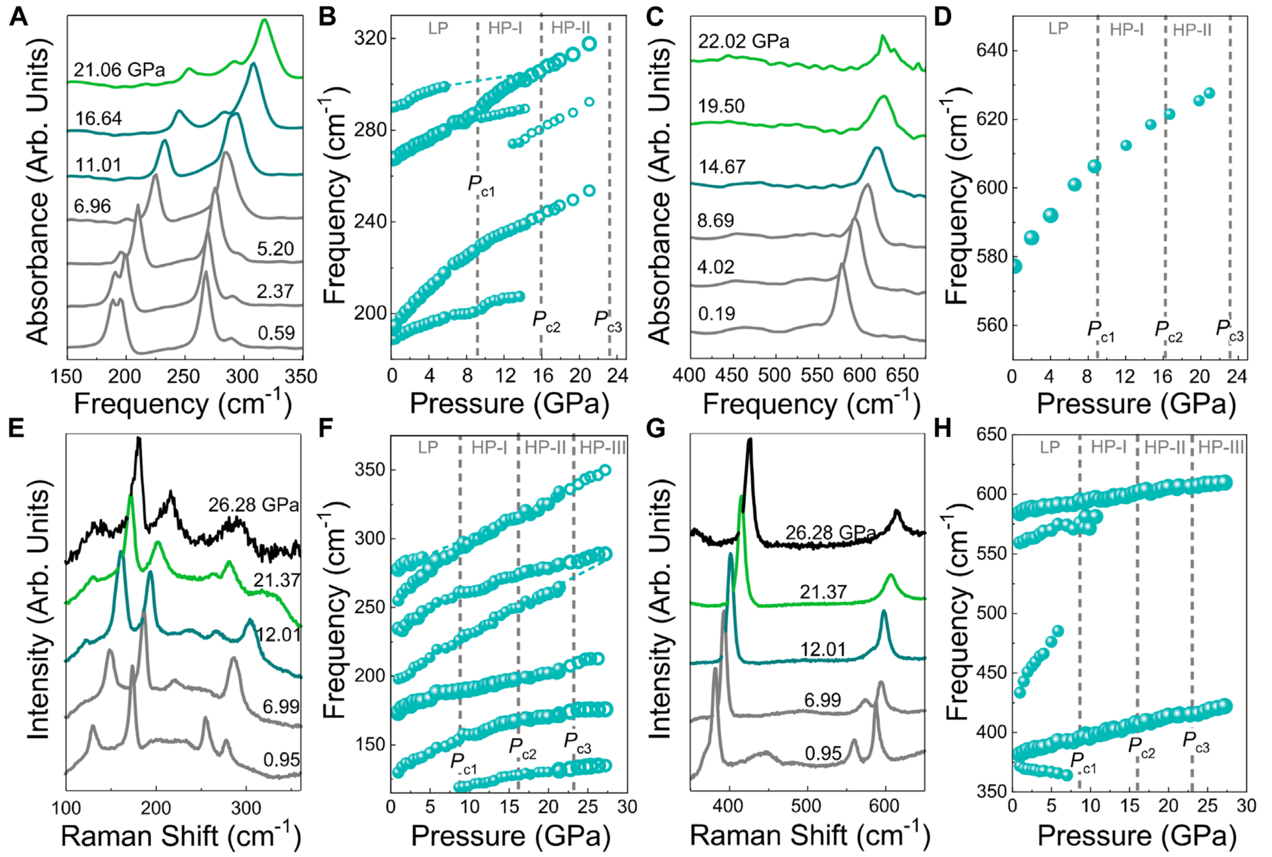

FIGURE 8
Vibrational properties of $NiPS_3$ under compression. **(A–D)** Close-up view of the infrared absorption and frequency vs. pressure plots. **(E–H)** Close-up view of the Raman scattering response and frequency vs. pressure plots. Spectra for the low pressure (LP) phase are shown in gray; those for the high pressure phases (HP-I, HP-II, and HP-III) are shown in teal, green, and black, respectively. Closed and open circles represent two independent runs. Note that infrared spectra in the HP-III phase are not included because the phonons are screened by the metallic response. The critical pressures (P_C's) separate the high pressure phases and are indicated with dashed vertical gray lines. Panels **(A–H)** from (Harms et al., 2022a).

very effective in this regard. It can even drive the ground state ferrimagnetic (Basnet et al., 2022a; Tezze et al., 2022). The magnetic properties of $NiPS_3$ are clearly very sensitive to chemical pressure, suggesting that there is more to learn under physical pressure. The latter is obviously a much cleaner technique as well. Light is also an important external stimuli in these materials. $NiPS_3$, for instance, sports laser-induced demagnetization with responsivity (lifetime) on the order of 10 ps (Kuntu et al., 2024). Photo-induced quenching of magnetic order is likely to be very sensitive to pressure.

Early high pressure x-ray diffraction work combined with first-principles calculations suggested strong similarities between $NiPS_3$ and the M = Mn and V analogs, with LP-to-HP-I and the HP-I-to-HP-II transitions near 15 and 27 GPa with an insulator-to-metal transition near 20 GPa (Ma et al., 2021). More recent efforts combining transport and x-ray diffraction reveal a series of different crystal structures under pressure, time-dependent and somewhat sluggish character to several of the transitions, and an insulator-to-metal transition near 30 GPa (Matsuoka et al., 2021). Systematic studies of hydrostatic pressure vs. strain demonstrates that the critical pressure of the insulator-to metal transition (as identified by transport measurements) is reduced from 30 to 12.5 GPa under uniaxial strain (Cui et al., 2021) - an observation that again emphasizes the need for hydrostatic pressure conditions. This confusing and somewhat contradictory picture was resolved by bringing together synchrotron-based infrared absorption, Raman scattering, x-ray diffraction, and first-principles calculations under pressure to show that in fact $NiPS_3$ is quite different from the other MPS_3 materials (Harms et al., 2022a) with a series of five different critical pressures. The set of symmetry progressions in this material is complex (involving $C2/m \rightarrow P\bar{3} \rightarrow P\bar{3}m1 \rightarrow P3m1 \rightarrow P3 \rightarrow P1$ space groups) from monoclinic to trigonal to noncentrosymmetric trigonal to triclinic phases (Figures 8, 9). The insulator-to-metal transition takes place near 23 GPa as evidenced by the development of a Drude response + screening of the phonons in the infrared spectrum. This definition of the insulator-to-metal transition obviously places the critical pressure below that obtained from a transport measurement (23 vs. 30 GPa), but the development of Drude signature in the electrodynamic response is an exquisitely sensitive indicator of metallicity. In any case, it's important to realize that several of the aforementioned space groups lack an inversion center, suggesting that $NiPS_3$ may be a polar metal under compression (Harms et al., 2022a). Whether the material is switchable (ferroelectric) or not switchable (pyroelectric)

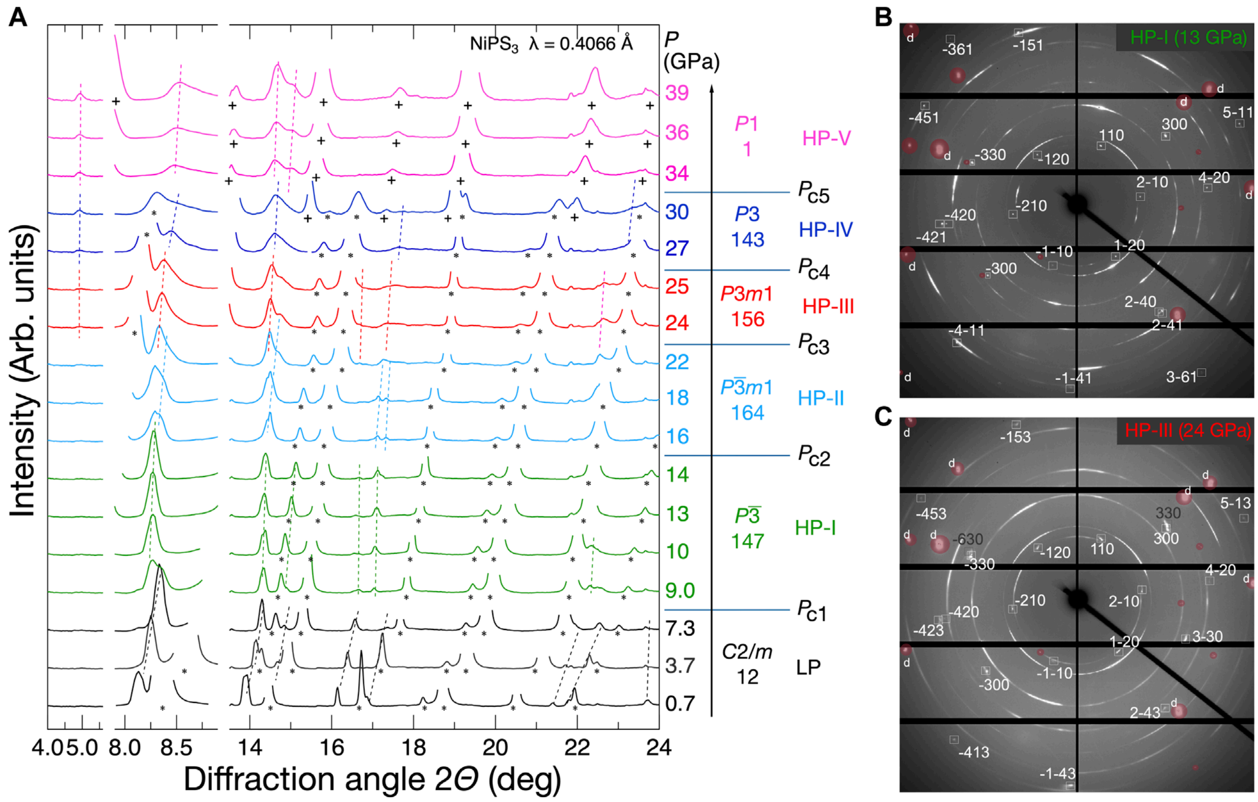

FIGURE 9
High pressure x-ray diffraction results of $NiPS_3$ up to 39 GPa. **(A)** Integrated x-ray diffraction profiles at indicated pressures. The appearance of x-ray diffraction peaks at the given angle are indicated, alongside dashed lines to guide the eye. Critical pressures, dividing individual pressure phases, are indicated by solid blue horizontal lines. The space groups of individual high pressure phases are labeled. The asterisk (∗) and plus (+) marks correspond to the diffraction response from NaCl in B1-type structure (below 30 GPa) and B2-type (above 30 GPa). **(B)** and **(C)** The x-ray diffraction images on the detector for HP-I (13 GPa) and HP-III (24 GPa). The peaks from $NiPS_3$ are enclosed with squares alongside the *hkl* indices for each phase. The gray labels in the panel **(C)** indicate the diffraction from HP-II. The Bragg diffraction from the diamond anvils is masked with red circles.Panels **(A–C)** from (Harms et al., 2022a).

under these conditions (in the $P3m1$ phase above 23 GPa) is unexplored at present. In principle, any electric polarization should increase as the space group progresses from $P3m1 \rightarrow P3 \rightarrow P1$ (Harms et al., 2022a; Aoyama et al., 2014). Real physical examples of polar metals are rare, so it's useful to consider how $NiPS_3$ hosts such a state when it has not been sighted (as of yet) in related MPX_3 systems. The current working hypothesis is that because $NiPS_3$ does not favor a $P\bar{3}m1$-type structure or layer-normal phosphorous chain formation, it may engage in negative charge transfer with hole formation at the S sites (Harms et al., 2022a). The optical properties of $NiPS_3$ have also been of sustained interest (Kim et al., 2018; Kang et al., 2020; Lane and Zhu, 2020)—both in single crystal and thin film form—although to our knowledge, there have been no studies under pressure or strain. Interestingly, electric field also drives an insulator-to-metal transition in the monolayer (Lane and Zhu, 2020), suggesting that pressure and electric field phase space may share more similarities that previously supposed.

$NiPSe_3$ is different, primarily because it does not have a complicated set of symmetry progressions under compression. Instead, there is a relatively simple structural sequence as shown in Figure 10 and Table 3, (Harms et al., 2022a; Sun et al., 2023). More recent efforts involving combined synchrotron x-ray diffraction and first-principles theory confirm these two structural transitions: LP to HP-I (where the honeycomb layers slide relative to each other) and HP-I to HP-II (where the structure has more three-dimensional character) (Sun et al., 2023). There is also a concomitant magnetic crossover at P_{C1} where the direction of the antiferromagnetic moment switches from out-of-plane to in-plane. Complementary resistance measurements indicate a bandwidth-controlled Mott insulator-metal transition near 8.0 GPa. The latter coincides with the emergence of superconductivity with $T_c \approx$ 4.8 K (Sun et al., 2023). This leads to a remarkable and complex pressure-temperature phase diagram hosting coexisting zigzag antiferromagnetic order and superconductivity (Figure 11).

Finally, we point out that transition metal dichalcogenides such as MoS_2 and WS_2 and related nanostructures are employed for solid state lubrication due to their ultra-low friction coefficients - especially under high shear conditions (Musfeldt et al., 2020). In an important initiative, Deng et al. (2024) are started to explore the mechanical properties of terenary chalcogenides like $NiPS_3$ using lateral force microscopy (Deng et al., 2024). These measurements reveal a friction coefficient of approximately

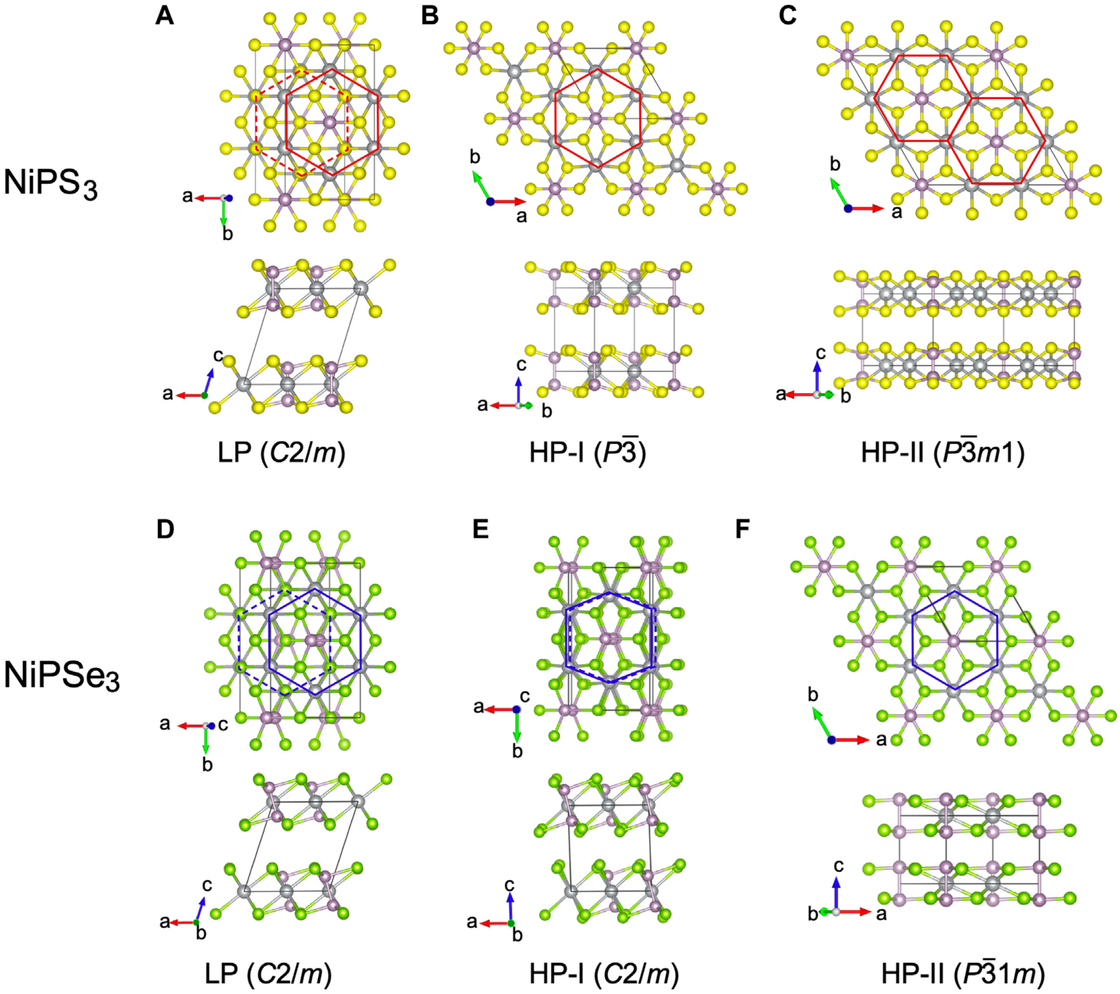

FIGURE 10
Crystal structures of $NiPS_3$ and $NiPSe_3$ in LP (**(A)** and **(D)**), HP-I (**(B)** and **(E)**), and HP-II (**(C)** and **(F)**) phases visualized using VESTA3 (Momma and Izumi, 2011) based on the experimental reports (Harms et al., 2022a; Sun et al., 2023). As discussed in the text, $NiPS_3$ displays an unusual sequence under pressure: $C2/m$ with $\beta \sim 108° \rightarrow P\bar{3} \rightarrow P\bar{3}m1 \rightarrow P31m$ and so on. This structural sequence is not seen in other members of the MPS_3 family. On the other hand, $NiPSe_3$ is similar to $FePS_3$ ($C2/m$ with $\beta \sim 108° \rightarrow C2/m$ with $\beta \sim 90° \rightarrow P\bar{3}1m$) and $MnPS_3$ ($C2/m$ with $\beta \sim 108° \rightarrow P\bar{3}1m$). The primary difference between the LP-phases of $NiPS_3$ and $NiPSe_3$ is the angle of the P-P dimer. The P-P dimer in $NiPS_3$ aligns almost perpendicular to the *ab* plane. On the other hand, the dimer in $NiPSe_3$ aligns mostly in an out-of-plane direction but with an angle.

4.5×10^{-3} under 5×10^{-3} Pa with load up to 768 nN. These findings are discussed in terms of the extremely weak interlayer interactions. Table 1 summarizes other candidates with low layer thickness/van der Waals gap ratios including $CdPS_3$ and $FePSe_3$ that should be tested.

2.4 $V_{1-x}PS_3$ ($x < 1$)

The vanadium phosphate synthesis has been achieved with the vanadium deficiency in $V_{1-x}PS_3$ which can be explained as due to valence mixing on the vanadium site between V^{2+} and V^{3+} states (Ouvrard et al., 1985b; Ichimura and Sano, 1991). The LP-phase has an electrical conductivity higher than 10^{-5} $\Omega^{(-1)}cm^{(-1)}$, while $MnPS_3$, $NIPS_3$ and $ZnPS_3$ crystals lower than 10^{-9} $\Omega^{(-1)}cm^{(-1)}$ at room temperature. The high conductivity of the former crystals is attributed to their mixed valency on the metal and/or the S and P sites, which has been revealed by x-ray photoelectron spectroscopy (Ichimura and Sano, 1991). The LP → HP-I transition starts at 2.6 GPa followed by the gradual transition to HP-I completing near 8.0 GPa (Coak et al., 2019). The layers of $V_{0.9}PS_3$ shift relative to each other in a sliding motion of $\sim a/3$ along the a-axis such that the S atoms become arranged in a hexagonal closed packing layout between the layers (Table 2; Figure 2), (Coak et al., 2019). In HP-I, P atoms are slightly distorted along the a-axis (the x coordinate value is 0.0074 at 17.7 GPa) of the unit cell, and this distortion results in the same $C2/m$ symmetry (Coak et al., 2019). The volume per formula unit decreases continuously without a sudden or discontinuous changes across the gradual LP → HP-I transformation (Figure 4). Coak et al. (2019) The electrical resistance decreases significantly and continuously with increasing pressure, and then the insulator-to-metal transition occurs near 12 GPa above the pressure where the LP → HP-I transformation completes (Coak et al., 2019). Thus, the isostructural insulator-to-metal transition is concluded,

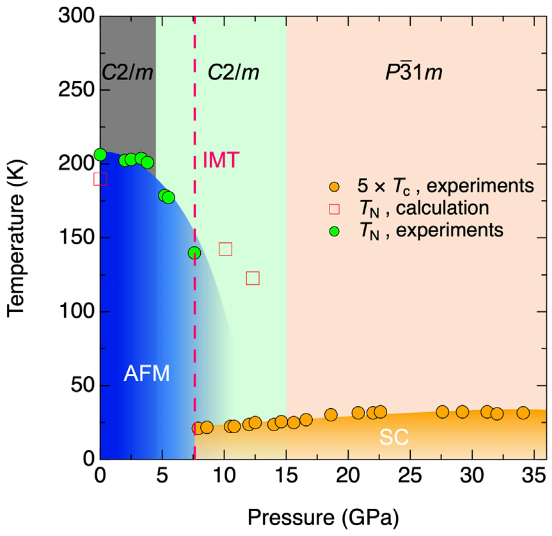

FIGURE 11
Phase diagram of $NiPSe_3$. Structural phase boundaries are from x-ray diffraction experiments at room temperature. T_N for AFM order and T_C for superconductivity are from electrical resistance measurements and DFT calculations. Created based on data from (Sun et al., 2023).

suggesting a second-order transition (Coak et al., 2019). From the magnetoresistance data, Coak et al. claim the insulator-to-metal transition involves the antiferromagnetic to paramagnetic transition (Coak et al., 2019). The R vs. T curve in the metallic phase shows an upturn at low temperatures. Coak et al. (2019) suggest that Kondo effect due to the vanadium deficiency and disordered valence mixing on the vanadium sites (Coak et al., 2019). The synthesis of $VPSe_3$ has not been reported to the knowledge of the authors.

2.5 $CoPS_3$ and $CoPSe_3$

Like other structural siblings, $CoPS_3$ has gained significant interest recently for the study of two-dimensional magnetism. Since Co^{2+} ion is in the d^7 configuration with a hole in the t_{2g} shell, significant effects of spin-orbit coupling on magnetism is expected. Indeed, recent theoretical studies suggested an interesting way to realize the so-called Kitaev's exchange interactions in cobalt-based compounds, (Kitaev, 2006; Liu and Khaliullin, 2018; Sano et al., 2018) which were originally considered in heavier transition metal systems (Jackeli and Khaliullin, 2009). Several Co-based systems including $CoPS_3$ have been studied for the search of the Kitaev-induced frustrated magnetism (Kim et al., 2020; Kim et al., 2021; Lin et al., 2021; Kim et al., 2023; Zhang et al., 2023). Considering the presence of metastable spin states and significant spin-orbit coupling in Co ions, (Yamaguchi et al,. 1996; Zobel et al., 2002). It is expected that pressure may induce intriguing evolution of electronic and magnetic properties of $CoPS_3$.

$CoPS_3$ crystallizes in $C2/m$ structure at ambient pressure as other MPS_3 family at ambient pressure. $CoPS_3$ exhibits AFM at ambient pressure with a $T_N = 122$ K and a Weiss temperature of $\theta = -166$ K (Ouvrard et al., 1982; Wildes et al., 2017). Single-crystal neutron diffraction shows that the magnetic propagation vector is $\boldsymbol{k} = [010]$ with the moments mostly along the a-axis and with a small component along the c-axis (Ouvrard et al., 1982; Wildes et al., 2017). As observed for $NiPS_3$, this magnetic structure is in sharp contrast to $MnPS_3$ and $FePS_3$ whose moments are mostly along the c-axis. Its effective moment is 4.9 μ_B, slightly larger than the expected value for a pure spin moment of a Co^{2+} cation (Ouvrard et al., 1982), implying orbital contribution to the magnetization as mentioned above. In addition, an inelastic neutron scattering study suggests a XXZ-type antiferromagneic order in $CoPS_3$, signalling the presence of the spin-orbit coupling-induced magnetic anisotropy (Kim et al., 2020).

High pressure properties of $CoPS_3$ have not been experimentally reported until recently, probably due to the significant difficulty in the synthesis and single crystal growth of this compound. A first-principles calculation from an article dedicated to the pressure effects in $CoPS_3$ predicts a pressure-driven isostructural Mott transition accompanied by a spin crossover (Gu et al. 2021). x-ray diffraction and Raman scattering measurements reveal that $CoPS_3$ exhibits $C2/m$ (LP) → $P\bar{3}$ (HP-I) structural transformation (Figure 2; Table 2) at 7 GPa and room temperature accompanied by the small drop (2.9%) of the volume per formula unit (Figure 4), (Matsuoka et al., 2023). This volume collapse and comparing $FePS_3$ and $MnPS_3$, it is concluded that $CoPS_3$ exhibits the spin crossover ($S = 3/2 \rightarrow 1/2$) accompanied by metallization. On the other hand, the 2.9% of volume collapse is much smaller than that of $FePS_3$ (10.6%) and $MnPS_3$ (19.7%) (Figure 4), (Wang et al., 2016; Wang et al., 2018b; Haines et al., 2018; Matsuoka et al., 2023). The ionic radii of high-spin (S = 3/2, 0.89 Å) and low-spin (S = 1/2, 0.79 Å) Co^{2+} ions make the high-spin → low-spin radius reduction 11.2%, which is not much smaller than that of Mn^{2+} (S = 5/2: 0.97 Å, S = 1/2: 0.81 Å, 16.5%) and Fe^{2+} (S = 2: 0.92 Å, S = 0: 0.75 Å, 18.5%) (Shannon, 1976). Thus, the slight volume reduction of $CoPS_3$ cannot be explained solely by the difference between high-spin and low-spin radii. It is also noticeable that the volume per formula unit and c-axis in the $P\bar{3}$ phase show a steeper compression between 7 and 12 GPa followed by moderate compression above 12 GPa, indicating a sign of structural stabilization (Matsuoka et al., 2023). These series of changes in compression behavior suggest an electronic transition in the $P\bar{3}$ phase. Upon decompression at room temperature, the $P\bar{3}$ phase remains down to 2 GPa revealing a large hysteresis in the volume per formula unit and c-axis. Concomitantly with the structural transition, the electrical resistance decreases significantly and $CoPS_3$ becomes metallic (Matsuoka et al., 2023). The positive Hall resistivity reveals this metallic $CoPS_3$ is a hole-dominant conductor with multiple conduction bands, and its non-saturating behavior against the external magnetic field, indicating the absence of the anomalous Hall effect, suggests that the metallic $CoPS_3$ is not ferromagnetic (Figure 12). The linear magnetoresistance $(\Delta\rho_{xy}(B)/\rho_{xx}(B=0)$, where $\Delta\rho_{xx}(B) = \rho_{xx}(B) - \rho_{xx}(B=0))$, along with the small volume collapse at the metallization, suggest the incomplete high-spin → low-spin transition in the metallic phase (Figure 12), (Matsuoka et al., 2023). It is expected that the metallic $CoPS_3$ possibly possesses an inhomogeneous magnetic moment distribution and short-range magnetic ordering (Matsuoka et al., 2023). Furthermore, the magnetoresistance changes from linear to

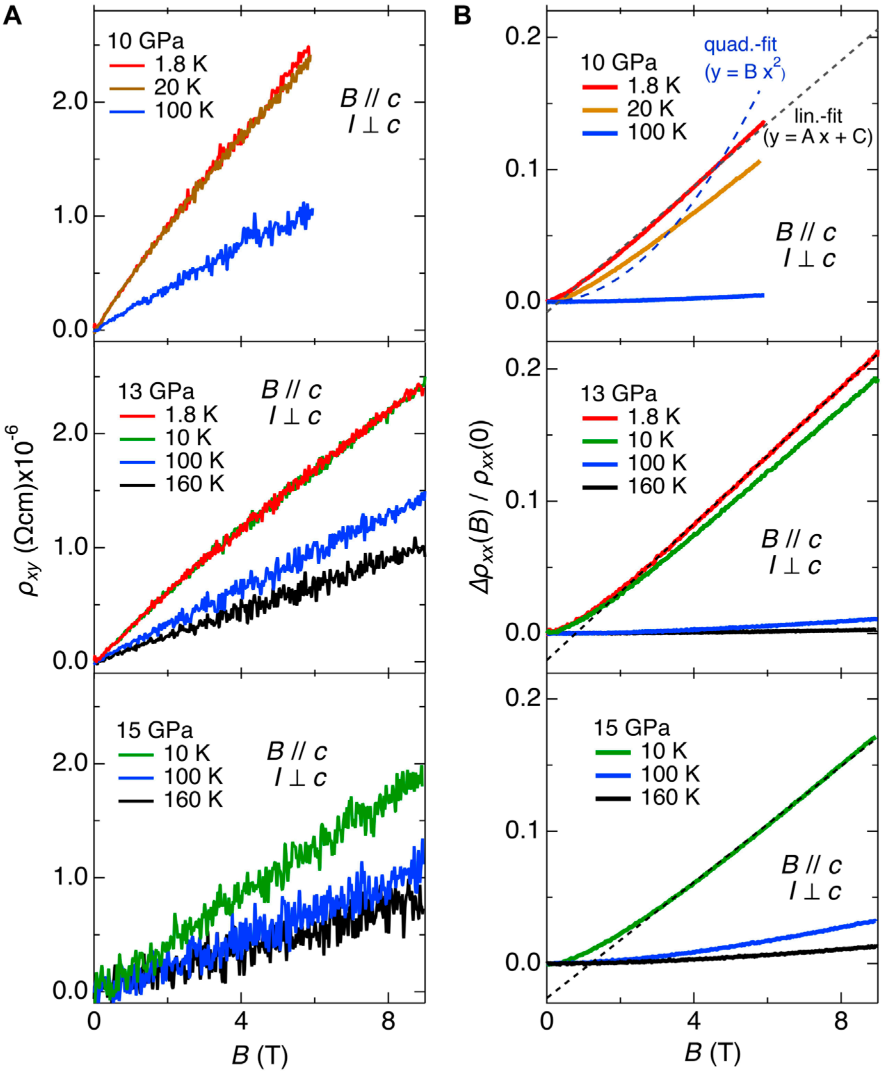

FIGURE 12
Transverse magnetotransport data from metallic $CoPS_3$. **(A)** The ρ_{xy} at different temperatures. The data at 1.8 K and 20 K at 10 GPa overlap (top panel). The data at 1.8 K and 10 K at 13 GPa overlap (middle panel). **(B)** The magnetoresistance. The dotted (black) and dashed (blue) lines in the top panel indicate the linear fit, $y = Ax + C$ and quadratic fits $y = Bx^2$ to the data at 10 GPa and 1.8 K (Matsuoka et al., 2023). Reprinted (Figure 5) with permission from [Matsuoka, T., Rao, R., Susner, M. A., Conner, B. S., Zhang, D., and Mandrus, D., Pressure-induced insulator-to-metal transition in the van der Waals compound $CoPS_3$, 107, 165125 (2023)).] Copyright (2023) by the American Physical Society.

more quadratic magnetic field dependent as pressure increases. Considering the suggested electronic transition from the volume per formula unit vs. pressure slope across 12 GPa (Figure 4), it can be thought that the spin crossover proceeds with pressure up to 12 GPa and stops or progress moderately above 12 GPa in the $P\bar{3}$ phase.

2.6 $CdPS_3$ and $CdPSe_3$

$CdPS_3$ crystallizes in the $C2/m$ structure with the monoclinic angle $\beta = 107.27°$, possessing an insulating electrical character like other MPX_3 family members (Ouvrard et al., 1985a; Niu et al., 2022). The Raman scattering measurements combined with *ab initio* calculation reveal that $CdPS_3$ exhibits two structural transformations the LP-phase ($C2/m$) → HP-I phase ($R\bar{3}$) that initiates near 0.11 GPa and completes near 1.1 GPa. The HP-I ($R\bar{3}$) → HP-II ($R\bar{3}$) transition occurs from 7.35 GPa to 10.2 GPa. Niu et al. (2022) the $C2/m \rightarrow R\bar{3}$ transition is obtained by sliding a single layer of the LP-phase along the b axis for a distance of about $b/6$ and simultaneously sliding it for approximately $a/3$ along the a axis. This results in the $C2/m$ unit's β angle changing from 107.27° to approximately 90° (Niu et al., 2022). The HP-I ($R\bar{3}$) to HP-II ($R\bar{3}$) transition is instead caused by the distortion of CdS_6 polyhedrons. The *ab initio* calculation suggests a small volume reduction (−2.05%) with the LP-I → HP-I transformation. On the other hand, the volume vs. pressure curves of HP-I and HP-II almost overlap across a wide pressure range (2–22 GPa), reflecting the transformation nature (Niu et al., 2022). The *ab initio*

TABLE 2 Crystal structures for the low pressure (LP) and high pressure (HP) phases of MPS_3.

	P (GPa)	Phase	Symmetry	Lattice constants	Ref.
$V_{0.9}PS_3$	1.1	LP	$C2/m$	$a = 5.8436(15)$ Å $b = 10.0876(8)$ Å $c = 6.5237(18)$ Å $\alpha = \gamma = 90°, \beta = 107.098(5)°$	Coak et al. (2019)
	1.8	HP-I	$C2/m$	$a = 5.5469(3)$ Å $b = 9.5892(6)$ Å $c = 5.4788(9)$ Å $\alpha = \gamma = 90°, \beta = 90.136(8)°$	Coak et al. (2019)
$MnPS_3$	0	LP	$C2/m$	$a = 6.077(1)$ Å $b = 10.524(3)$ Å $c = 6.796(1)$ Å $\alpha = \gamma = 90°, \beta = 107.35(2)°$	Ouvrard et al. (1985a)
	12	HP-I	$P\bar{3}1m$	$a = b = 5.725$ Å $c = 5.758$ Å $\alpha = \beta = 90°, \gamma = 120°$	Harms et al. (2020)
	33	HP-II	$C2/m$	$a = 4.858(3)$ Å $b = 8.171(5)$ Å $c = 6.263(3)$ Å $\alpha = \beta = 90°, \gamma = 107.98°$	Wang et al. (2016)
$FePS_3$	0	LP	$C2/m$	$a = 5.9428(9)$ Å $b = 10.299(2)$ Å $c = 6.716(2)$ Å $\alpha = \gamma = 90°, \beta = 107.34(2)°$	Haines et al. (2018)
	10	HP-I	$C2/m$	$a = 5.7620(12)$ Å $b = 9.988(2)$ Å $c = 5.803(5)$ Å $\alpha = \beta = 90°, \gamma = 89.33(2)°$	Haines et al. (2018)
	18	HP-II	$P\bar{3}m1$	$a = b = 5.699(4)$ Å $c = 4.818(3)$ Å $\alpha = \beta = 90°, \gamma = 120°$	Haines et al. (2018)

(Continued on the following page)

TABLE 2 (*Continued*) Crystal structures for the low pressure (LP) and high pressure (HP) phases of MPS_3.

	P (GPa)	Phase	Symmetry	Lattice constants	Ref.
$CoPS_3$	0.5	LP	$C2/m$	$a = 5.844(1)$ Å $b = 10.127(1)$ Å $c = 6.562(4)$ Å $\alpha = \beta = 90°, \gamma = 107.04(2)°$	Matsuoka et al. (2023)
	17	HP-I	$P\bar{3}$	$a = b = 5.570(5)$ Å $c = 5.13(2)$ Å $\alpha = \beta = 90°, \gamma = 120°$	Matsuoka et al. (2023)
$NiPS_3$	0.7	LP	$C2/m$	$a = 5.800(1)$ Å $b = 10.057(1)$ Å $c = 6.605(2)$ Å $\alpha = \gamma = 90°, \beta = 106.99(2)°$	Harms et al. (2022a)
	13	HP-I	$P\bar{3}$	$a = b = 5.638(5)$ Å $c = 5.88(2)$ Å $\alpha = \beta = 90°, \gamma = 120°$	Harms et al. (2022a)
	16	HP-II	$P\bar{3}m1$	$a = b = 9.720(1)$ Å $c = 4.94(1)$ Å $\alpha = \beta = 90°, \gamma = 120°$	Harms et al. (2022a)
	24	HP-III	$P3m1$	$a = b = 5.582(3)$ Å $c = 15.03(2)$ Å $\alpha = \beta = 90°, \gamma = 120°$	Harms et al. (2022a)
	27	HP-IV	$P3$	$a = b = 5.488(1)$ Å $c = 9.92(4)$ Å $\alpha = \beta = 90°, \gamma = 120°$	Harms et al. (2022a)
$CdPS_3$	0	LP	$C2/m$	$a = 6.218(1)$ Å $b = 10.763(2)$ Å $c = 6.867(1)$ Å $\alpha = \gamma = 90°, \beta = 107.58(1)°$	Ouvrard et al. (1985a)

calculation also suggests the further transformation from HP-II to HP-III ($P\bar{3}1m$) at approximately 25 GPa. Compared with other MPS_3, it is noticeable that the LP-phase of $CdPS_3$ is relatively more sensitive to external pressure than other MPX_3 reported so far LP → HP-I at 0.11 GPa. This would suggest that even a slight strain can be an effective stimulus to drive the appearance of a new structural phase of $CdPS_3$. Finally, we note that the M = Cd system may prove a useful platform for exploring spin-orbit coupling, although it will require analogous measurements to be made on $ZnPS_3$ and $ZnPSe_3$ for comparison.

TABLE 3 Crystal structures for the low pressure (LP) and high pressure (HP) phases of $MPSe_3$.

	P (GPa)	Phase	Symmetry	Lattice constants	Ref.
$MnPSe_3$	0	LP	$R\bar{3}$	$a = b = 6.387(2)$Å $c = 19.996(6)$ Å $\alpha = \beta = 90°, \gamma = 120°$	Wiedenmann et al. (1981)
	27	HP-I	$C2/m$	$a = 5.266(3)$ Å $b = 7.600(5)$ Å $c = 7.151(3)$ Å $\alpha = \gamma = 90°, \beta = 108.17°$	Wang et al. (2016)
$FePSe_3$	0	LP	$R\bar{3}$	$a = b = 6.262(3)$ Å $c = 6.716(2)$ Å $\alpha = \beta = 90°, \gamma = 120°$	Wiedenmann et al. (1981) Liu et al. (2022)
	18	HP-I	$R\bar{3}$	$a = b = 5.824$ Å $c = 19.330$ Å $\alpha = \beta = 90°, \gamma = 120°$	Wang et al. (2018b)
$NiPSe_3$	2.2	LP	$C2/m$	$a = 6.052(1)$ Å $b = 10.440(1)$ Å $c = 6.705(1)$ Å $\alpha = \gamma = 90°, \beta = 108.45(2)°$	Sun et al. (2023)
	6.3	HP-I	$C2/m$	$a = 5.898(1)$Å $b = 10.348(1)$ Å $c = 6.303(1)$ Å $\alpha = \gamma = 90°, \beta = 88.38(1)°$	Sun et al. (2023)
	25.7	HP-II	$P\bar{3}1m$	$a = b = 5.873(2)$ Å $c = 4.274(4)$ Å $\alpha = \beta = 90°, \gamma = 120°$	Sun et al. (2023)

3 Summary and future prospects

Complex chalcogenides display properties and states of matter that are incredibly sensitive to external stimuli. This particular review is inspired by opportunities to employ pressure to unveil elusive states of matter and uncover charge-structure-function relationships. Compression is particularly well-suited to tuning the properties of chalcogenides because, in addition to changing bond lengths and angles, it provides deterministic control of the c/a structural ratio and the van der Waals gap. By controlling the environment around the metal center, compression also controls spin. As emphasized throughout this review, strain is likely to offer complementary advantages. At the same time, expanding the chemical phase space of the MPX_3 system to include solid solutions like $(Zn,Cd)PS_3$ or $(Ni,Co)PS_3$, heavy 4- and 5d-metal centers to enhance spin-orbit coupling, the $CrPS_4$ member of this family, and dual sublattice analogs such as bimetallic $CuInP_2S_6$ and $AgInP_2S_6$ provides exciting new platforms for exploring ferroelectricity, new types of photoinduced behavior, ionic motion, and even charge pumping under compression.

Author contributions

TM: Funding acquisition, Visualization, Writing–original draft, Writing–review and editing. H-SK: Visualization, Writing–original draft, Writing–review and editing, Funding acquisition. SS: Writing–original draft, Writing–review and editing. JM: Funding acquisition, Visualization, Writing–original draft, Writing–review and editing. DM: Funding acquisition, Visualization, Writing–original draft, Writing–reviewand editing.

Funding

The authors declare that financial support was received for the research, authorship, and/or publication of this article. TM is supported by the Air Force Office of Scientific Research under award number FA2386-23-1-4112, Dr. Emerlinda Roman Professorial Chair Grant awarded from University of the Philippines Foundation (2023–2024), and the NIP research contract (2023). HSK and SS are funded by the Korea Research Fellow (KRF) Program and the Basic Science Research Program through the National Research Foundation of Korea funded by the Ministry of Education (Grant No. NRF-2019H1D3A1A01102984, 424 NRF-2020R1C1C1005900, and RS-2023-00220471). JLM is funded by Physical Behavior of Materials, Basic Energy Sciences, U.S. Department of Energy (Contract number DE-SC00023144). DGM is funded by the Gordon and Betty Moore Foundation's EPiQS Initiative, Grant No. GBMF9069.

Acknowledgments

The authors thank our collaborators for valuable discussions: Dr. Nathan C. Harms, Dr. Amanda Haglund, Dr. Amanda J. Clune, Dr. Rui Xue, Dr. Kevin A. Smith, Dr. Kenneth R. O'Neal, and Dr. Maik Lang from The University of Tennesee Knoxville, Dr. Jesse S. Smith and Dr. Dongzhou Zhang from Argonne National Laboratory, Dr. Erxi Feng, Dr. Huibo Cao, and Dr. Antonio M. dos Santos from Oak Ridge National Laboratory, Dr. Rahul Rao, Dr. Michael A. Susner, and Dr. Benjamin S. Conner from Air Force Research Laboratory, Dr. Zhenxian Liu from The University of Illinois Chicago, Dr. Kristjan Haule and Dr. David Vanderbilt from Rutgers University.

Conflict of interest

The authors declare that the research was conducted in the absence of any commercial or financial relationships that could be construed as a potential conflict of interest.

Publisher's note

References

Afanasiev, D., Hortensius, J. R., Matthiesen, M., Mañas-Valero, S., Šiškins, M., Lee, M., et al. (2021). Controlling the anisotropy of a van der Waals antiferromagnet with light. *Sci. Adv.* 7, eabf3096. doi:10.1126/sciadv.abf3096

Aoyama, T., Yamauchi, K., Iyama, A., Picozzi, S., Shimizu, K., and Kimura, T. (2014). Giant spin-driven ferroelectric polarization in $TbMnO_3$ under high pressure. *Nat. Commun.* 5, 4927. doi:10.1038/ncomms5927

Basnet, R., Ford, D., TenBarge, K., Lochala, J., and Hu, J. (2022a). Emergence of ferrimagnetism in Li-intercalated $NiPS_3$. *J. Phys. Condens. Matter* 34, 434002. doi:10.1088/1361-648X/ac8a81

Basnet, R., Kotur, K. M., Rybak, M., Stephenson, C., Bishop, S., Autieri, C., et al. (2022b). Controlling magnetic exchange and anisotropy by nonmagnetic ligand substitution in layered MPX_3 (M= Ni, Mn; X= S, Se). *Phys. Rev. Res.* 4, 023256. doi:10.1103/physrevresearch.4.023256

Basnet, R., Wegner, A., Pandey, K., Storment, S., and Hu, J. (2021). Highly sensitive spin-flop transition in antiferromagnetic van der Waals material MPS_3 (M = Ni and Mn). *Phys. Rev. Mater.* 5, 064413. doi:10.1103/PhysRevMaterials.5.064413

Bhutani, A., Zuo, J. L., McAuliffe, R. D., dela Cruz, C. R., and Shoemaker, D. P. (2020). Strong anisotropy in the mixed antiferromagnetic system $Mn_{1-x}Fe_xPSe_3$. *Phys. Rev. Mater.* 4, 034411. doi:10.1103/PhysRevMaterials.4.034411

Boerio-Goates, J., Lifshitz, E., and Francis, A. H. (1981). Electronic spectroscopy of nearly octahedrally coordinated manganese in manganese phosphide sulfide ($MnPS_3$) and cadmium phosphide sulfide ($CdPS_3$) lattices. *Inorg. Chem.* 20, 3019–3023. doi:10.1021/ic50223a052

Burch, K. S., Mandrus, D., and Park, J.-G. (2018). Magnetism in two-dimensional van der waals materials. *Nature* 563, 47–52. doi:10.1038/s41586-018-0631-z

Butler, C., Yoshida, M., Hanaguri, T., and Iwasa, Y. (2020). Mottness versus unit-cell doubling as the driver of the insulating state in 1T-TaS_2. *Nat. Commun.* 11, 2477. doi:10.1038/s41467-020-16132-9

Chandrasekharan, N., and Vasudevan, S. (1994). Magnetism and exchange in the layered antiferromagnet $NiPS_3$. *J. Phys. Condens. Matter* 6, 4569–4579. doi:10.1088/0953-8984/6/24/017

Coak, M. J., Jarvis, D. M., Hamidov, H., Haines, C. R. S., Alireza, P. L., Liu, C., et al. (2020). Tuning dimensionality in van-der-Waals antiferromagnetic Mott insulators $TMPS_3$. *J. Phys. Condens. Matter* 32, 124003. doi:10.1088/1361-648X/ab5be8

Coak, M. J., Jarvis, D. M., Hamidov, H., Wildes, A. R., Paddison, J. A. M., Liu, C., et al. (2021). Emergent magnetic phases in pressure-tuned van der Waals antiferromagnet $FePS_3$. *Phys. Rev. X* 11, 011024. doi:10.1103/PhysRevX.11.011024

Coak, M. J., Son, S., Daisenberger, D., Hamidov, H., Haines, C. R. S., Alireza, P. L., et al. (2019). Isostructural Mott transition in 2D honeycomb antiferromagnet $V_{0.9}PS_3$. *npj Quantum Mater.* 4, 38. doi:10.1038/s41535-019-0178-8

Cui, H., Yun, S., Lee, K. J., Lee, C., Chang, S. H., Lee, Y., et al. (2021). Quasihydrostatic versus nonhydrostatic pressure effects on the electrical properties of $NiPS_3$. *Phys. Rev. Mater.* 5, 124008. doi:10.1103/PhysRevMaterials.5.124008

Dedkov, Y., Guo, Y., and Voloshina, E. (2023). Progress in the studies of electronic and magnetic properties of layered MPX_3 materials (M: transition metal, X: chalcogen). *Electron. Struct.* 5, 043001. doi:10.1088/2516-1075/acfa4e

Deng, H., Yu, T., Du, C., Shen, R., Zhao, Y., He, X., et al. (Friction, under review, (2024)). $NiPS_3$: a ternary 2D material with an ultra-low friction coefficient.

Deng, S., Chen, S., Monserrat, B., Artacho, E., and Saxena, S. S. (2023). Pressure-induced transitions in $FePS_3$: structural, magnetic and electronic properties. *SciPost Phys.* 15, 020. doi:10.21468/SciPostPhys.15.1.020

Friedel, M. C. (1894). Sur une nouvelle série de sulfophosphures, les thiohypophosphates. *Comptes rendus l'Académie Sci.* 119, 260–264.

Fujii, M., Yamaguchi, T., Ohkochi, T., De, C., Cheong, S.-W., and Mizokawa, T. (2022). Bulk and surface electronic structure of $MnPSe_3$ revealed by photoemission and x-ray absorption spectroscopy. *Phys. Rev. B* 106, 035118. doi:10.1103/PhysRevB.106.035118

Grasso, V., Neri, F., Perillo, P., Silipigni, L., and Piacentini, M. (1991). Optical-absorption spectra of crystal-field transitions in $MnPS_3$ at low temperatures. *Phys. Rev. B* 44, 11060–11066. doi:10.1103/PhysRevB.44.11060

Gu, Y., Zhang, S., and Zou, X. (2021). Tunable magnetism in layered $CoPS_3$ by pressure and carrier doping. *Sci. China Mater.* 64, 673–682. doi:10.1007/s40843-020-1453-0

Haines, C. R. S., Coak, M. J., Wildes, A. R., Lampronti, G. I., Liu, C., Nahai-Williamson, P., et al. (2018). Pressure-induced electronic and structural phase evolution in the van der Waals compound $FePS_3$. *Phys. Rev. Lett.* 121, 266801. doi:10.1103/PhysRevLett.121.266801

Harms, N. C., Kim, H.-s., Clune, A. J., Smith, K. A., O'Neal, K. R., Haglund, A. V., et al. (2020). Piezochromism in the magnetic chalcogenide $MnPS_3$. *npj Quantum Mater.* 5, 56. doi:10.1038/s41535-020-00259-5

Harms, N. C., Matsuoka, T., Samanta, S., Clune, A. J., Smith, K. A., Haglund, A. V., et al. (2022a). Symmetry progression and possible polar metallicity in $NiPS_3$ under pressure. *npj 2D Mater. Appl.* 6, 40. doi:10.1038/s41699-022-00313-9

Harms, N. C., Smith, K. A., Haglund, A. V., Mandrus, D. G., Liu, Z., Kim, H.-s., et al. (2022b). Metal site substitution and role of the dimer on symmetry breaking in $FePS_3$ and $CrPS_4$ under pressure. *ACS Appl. Electron. Mater.* 4, 3246–3255. doi:10.1021/acsaelm.2c00563

Hiroi, Z. (2008). A brief comment on the chemical formulae of the rare earth iron arsenide oxide superconductors. *arXiv0805.4668*. doi:10.48550/arXiv.0805.4668

Ichimura, K., and Sano, M. (1991). Electrical conductivity of layered transition-metal phosphorus trisulfide crystals. *Synth. Met.* 45, 203–211. doi:10.1016/0379-6779(91)91804-J

Jackeli, G., and Khaliullin, G. (2009). Mott insulators in the strong spin-orbit coupling limit: from Heisenberg to a quantum compass and Kitaev models. *Phys. Rev. Lett.* 102, 017205. doi:10.1103/PhysRevLett.102.017205

Jophnson, J. W., and Jacobson, A. (1982). "Intercalation chemistry of metal phosphorus trichalcogenides," in *Intercalation chemistry* (Academic Press Inc New York), 267–283.

Joy, P. A., and Vasudevan, S. (1992). Magnetism in the layered transition-metal thiophosphates MPS_3 (M =Mn, Fe, and Ni). *Phys. Rev. B* 46, 5425–5433. doi:10.1103/PhysRevB.46.5425

Kang, S., Kim, K., Kim, B. H., Kim, J., Sim, K. I., Lee, J.-U., et al. (2020). Coherent many-body exciton in van der Waals antiferromagnet $NiPS_3$. *Nature* 583, 785–789. doi:10.1038/s41586-020-2520-5

Kargar, F., Aytan, E., Ghosh, S., Lee, J., Gomez, M., Liu, Y., et al. (2019). Phonon and thermal properties of quasi-two-dimensional $FePS_3$ and $MnPS_3$ antiferromagnetic semiconductor materials. *ACS Nano* 14, 2424–2435. doi:10.1021/acsnano.9b09839

Kim, C., Jeong, J., Lin, G., Park, P., Masuda, T., Asai, S., et al. (2021). Antiferromagnetic kitaev interaction in J_{eff} = 1/2 cobalt honeycomb materials $Na_3Co_2SbO_6$ and $Na_2Co_2TeO_6$. *J. Phys. Condens. Matter* 34, 045802. doi:10.1088/1361-648X/ac2644

Kim, C., Jeong, J., Park, P., Masuda, T., Asai, S., Itoh, S., et al. (2020). Spin waves in the two-dimensional honeycomb lattice xxz-type van der waals antiferromagnet $CoPS_3$. *Phys. Rev. B* 102, 184429. doi:10.1103/PhysRevB.102.184429

Kim, C., Kim, S., Park, P., Kim, T., Jeong, J., Ohira-Kawamura, S., et al. (2023). Bond-dependent anisotropy and magnon decay in cobalt-based Kitaev triangular antiferromagnet. *Nat. Phys.* 19, 1624–1629. doi:10.1038/s41567-023-02180-7

Kim, H.-S., Haule, K., and Vanderbilt, D. (2019). Mott metal-insulator transitions in pressurized layered trichalcogenides. *Phys. Rev. Lett.* 123, 236401. doi:10.1103/PhysRevLett.123.236401

Kim, M., Kim, H.-S., Haule, K., and Vanderbilt, D. (2022). Orbital-selective mott phase and non-Fermi liquid in $FePS_3$. *Phys. Rev. B* 105, L041108. doi:10.1103/PhysRevB.105.L041108

Kim, S. Y., Kim, T. Y., Sandilands, L. J., Sinn, S., Lee, M. C., Son, J., et al. (2018). Charge-spin correlation in van der Waals antiferromagnet $NiPS_3$. *Phys. Rev. Lett.* 120, 136402. doi:10.1103/PhysRevLett.120.136402

Kitaev, A. (2006). Anyons in an exactly solved model and beyond. *Ann. Phys.* 321, 2–111. January Special Issue. doi:10.1016/j.aop.2005.10.005

Klingen, W., Ott, R., and Hahn, H. (1973). Uber die darstellung und eigenschaften von hexathio-und hexaselenohypodiphosphaten. *Z. für Anorg. Allg. Chem.* 396, 271–278. doi:10.1002/zaac.19733960305

Kuntu, D. V., Arkhipova, E. A., Shelukhin, L. A., Mertens, F., Prosnikov, M. A., Eliseyev, I. A., et al. (2024). Laser-induced demagnetization in van der Waals XY- and ising-like antiferromagnets $NiPS_3$ and $FePS_3$. *Phys. Rev. Mat.* 8, 014408. doi:10.1103/PhysRevMaterials.8.014408

Kurosawa, K., Saito, S., and Yamaguch, Y. (1983a). Neutron diffraction study on $MnPS_3$ and $FePS_3$. *J. Phys. Soc. Jpn.* 52, 3919–3926. doi:10.1143/JPSJ.52.3919

Kurosawa, K., Saito, S., and Yamaguchi, Y. (1983b). Neutron diffraction study on $MnPS_3$ and $FePS_3$. *J. Phys. Soc. Jpn.* 52, 3919–3926. doi:10.1143/JPSJ.52.3919

Lançon, D., Walker, H. C., Ressouche, E., Ouladdiaf, B., Rule, K. C., McIntyre, G. J., et al. (2016). Magnetic structure and magnon dynamics of the quasi-two-dimensional antiferromagnet $FePS_3$. *Phys. Rev. B* 94, 214407. doi:10.1103/PhysRevB.94.214407

Lane, C., and Zhu, J.-X. (2020). Thickness dependence of electronic structure and optical properties of a correlated van der Waals antiferromagnetic $NiPS_3$ thin film. *Phys. Rev. B* 102, 075124. doi:10.1103/PhysRevB.102.075124

Lee, J.-U., Lee, S., Ryoo, J. H., Kang, S., Kim, T. Y., Kim, P., et al. (2016). Ising-type magnetic ordering in atomically thin $FePS_3$. *Nano Lett.* 16, 7433–7438. doi:10.1021/acs.nanolett.6b03052

Le Flem, G., Brec, R., Ouvard, G., Louisy, A., and Segransan, P. (1982). Magnetic interactions in the layer compounds MPX_3 (M = Mn, Fe, Ni; X = S, Se). *J. Phys. Chem. Solids* 43, 455–461. doi:10.1016/0022-3697(82)90156-1

Lin, G., Jeong, J., Kim, C., Wang, Y., Huang, Q., Masuda, T., et al. (2021). Field-induced quantum spin disordered state in spin−1/2 honeycomb magnet $Na_2Co_2TeO_6$. *Nat. Commun.* 12, 5559. doi:10.1038/s41467-021-25567-7

Liu, B., Yang, Y., Fu, Y., and He, J. (2022). Study on physical properties of two-dimensional layered magnetic semiconductor material $FePSe_3$. *Adv. Condens. Matter Phys.* 11, 21–27. doi:10.12677/CMP.2022.112003

Liu, H., and Khaliullin, G. (2018). Pseudospin exchange interactions in d^7 cobalt compounds: possible realization of the Kitaev model. *Phys. Rev. B* 97, 014407. doi:10.1103/PhysRevB.97.014407

Lu, Z., Yang, X., Huang, L., Chen, X., Liu, M., Peng, J., et al. (2022). Evolution of magnetic phase in two-dimensional van der Waals $Mn_{1-x}Ni_xPS_3$ single crystals. *J. Phys. Condens. Matter* 34, 354005. doi:10.1088/1361-648X/ac7a80

Ma, X., Wang, Y., Yin, Y., Yue, B., Dai, J., Cheng, J., et al. (2021). Dimensional crossover tuned by pressure in layered magnetic $NiPS_3$. *Sci. China Phys. Mech. I& Astronomy* 64, 297011. doi:10.1007/s11433-021-1727-6

Mai, T. T., Garrity, K. F., McCreary, A., Argo, J., Simpson, J. R., Doan-Nguyen, V., et al. (2021). Magnon-phonon hybridization in 2D antiferromagnet $MnPSe_3$. *Sci. Adv.* 7, eabj3106–7. doi:10.1126/sciadv.abj3106

Matsuoka, T., Haglund, A., Xue, R., Smith, J. S., Lang, M., dos Santos, A. M., et al. (2021). Pressure-induced insulator–metal transition in two-dimensional mott insulator $NiPS_3$. *J. Phys. Soc. Jpn.* 90, 124076. doi:10.7566/JPSJ.90.124706

Matsuoka, T., Rao, R., Susner, M. A., Conner, B. S., Zhang, D., and Mandrus, D. (2023). Pressure-induced insulator-to-metal transition in the van der Waals compound $CoPS_3$. *Phys. Rev. B* 107, 165125. doi:10.1103/PhysRevB.107.165125

Mehlawat, K., Alfonsov, A., Selter, S., Shemerliuk, Y., Aswartham, S., Büchner, B., et al. (2022). Low-energy excitations and magnetic anisotropy of the layered van der Waals antiferromagnet $Ni_2P_2S_6$. *Phys. Rev. B* 105, 214427. doi:10.1103/PhysRevB.105.214427

Momma, K., and Izumi, F. (2011). *VESTA3* for three-dimensional visualization of crystal, volumetric and morphology data. *J. Appl. Crystallogr.* 44, 1272–1276. doi:10.1107/S0021889811038970

Musfeldt, J. L., Iwasa, Y., and Tenne, R. (2020). Nanotubes from layered transition metal dichalcogenides. *Phys. Today* 73, 42–48. doi:10.1063/PT.3.4547

Musfeldt, J. L., Mandrus, D. G., and Liu, Z. (2023). Insulator–metal transition in $CrSiTe_3$ triggered by structural distortion under pressure. *npj 2D Mater. Appl.* 7, 28–36. doi:10.1038/s41699-023-00389-x

Nauman, M., Kiem, D. H., Lee, S., Son, S., Park, J.-G., Kang, W., et al. (2021). Complete mapping of magnetic anisotropy for prototype ising van der waals $FePS_3$. *2D Mater.* 8, 035011. doi:10.1088/2053-1583/abeed3

Neal, S. N., Kim, H.-S., O'Neal, K. R., Haglund, A. V., Smith, K. A., Mandrus, D. G., et al. (2020). Symmetry crossover in layered MPS_3 complexes (M = Mn, Fe, Ni). *Phys. Rev. B* 102, 085408. doi:10.1103/PhysRevB.102.085408

Neal, S. N., Kim, H.-S., Smith, K. A., Haglund, A. V., Mandrus, D. G., Bechtel, H. A., et al. (2019). Near-field infrared spectroscopy of monolayer $MnPS_3$. *Phys. Rev. B* 100, 075428. doi:10.1103/PhysRevB.100.075428

Niu, M., Cheng, H., Li, X., Yu, J., Yang, X., Gao, Y., et al. (2022). Pressure-induced phase transitions in weak interlayer coupling $CdPS_3$. *Appl. Phys. Lett.* 120, 233104. doi:10.1063/5.0089478

Ouvrard, G., Brec, R., and Rouxel, J. (1982). Synthesis and physical characterization of the lamellar compound $CoPS_3$. *Chem. Inf.* 13, 971. doi:10.1002/chin.198235037

Ouvrard, G., Brec, R., and Rouxel, J. (1985a). Structural determination of some MPS_3 layered phases (M = Mn, Fe, Co, Ni and Cd). *Mater. Res. Bull.* 20, 1181–1189. doi:10.1016/0025-5408(85)90092-3

Ouvrard, G., Fréour, R., Brec, R., and Rouxel, J. (1985b). A mixed valence compound in the two dimensional MPS_3 family: $V_{0.78}PS_3$ structure and physical properties. *Mater. Res. Bull.* 20, 1053–1062. doi:10.1016/0025-5408(85)90204-1

Park, K., Mandrus, D., Kim, H. S., and Musfeldt, J. L. (2024). *Unpublished work*.

Pei, Q., Wang, X.-C., Zou, J.-J., and Mi, W.-B. (2018). Tunable electronic structure and magnetic coupling in strained two-dimensional semiconductor $MnPSe_3$. *Front. Phys.* 13, 137105. doi:10.1007/s11467-018-0796-9

Pei, S., Wang, Z., and Xia, J. (2022). High pressure studies of 2D materials and heterostructures: a review. *Mater. Des.* 213, 110363. doi:10.1016/j.matdes.2021.110363

Peng, J., Yang, X., Lu, Z., Huang, L., Chen, X., He, M., et al. (2023). Ferromagnetism induced by magnetic dilution in van der Waals material metal thiophosphates. *Adv. Quantum Technol.* 6, 2200105. doi:10.1002/qute.202200105

Ressouche, E., Loire, M., Simonet, V., Ballou, R., Stunault, A., and Wildes, A. (2010). Magnetoelectric $MnPS_3$ as a candidate for ferrotoroidicity. *Phys. Rev. B* 82, 100408. doi:10.1103/PhysRevB.82.100408

Sano, R., Kato, Y., and Motome, Y. (2018). Kitaev-Heisenberg Hamiltonian for high-spin d^7 mott insulators. *Phys. Rev. B* 97, 014408. doi:10.1103/PhysRevB.97.014408

Shannon, R. D. (1976). Revised effective ionic radii and systematic studies of interatomic distances in halides and chalcogenides. *Acta Crystallogr. Sect. A* 32, 751–767. doi:10.1107/S0567739476001551

Sun, H., Qiu, L., Han, Y., Yi, E., Li, J., Huo, M., et al. (2023). Coexistence of zigzag antiferromagnetic order and superconductivity in compressed $NiPSe_3$. *Mater. Today Phys.* 36, 101188. doi:10.1016/j.mtphys.2023.101188

Sun, Y. J., Tan, Q. H., Liu, X. L., Gao, Y. F., and Zhang, J. (2019). Probing the magnetic ordering of antiferromagnetic $MnPS_3$ by Raman spectroscopy. *J. Phys. Chem. Lett.* 10, 3087–3093. doi:10.1021/acs.jpclett.9b00758

Tezze, D., Pereira, J. M., Asensio, Y., Ipatov, M., Calavalle, F., Casanova, F., et al. (2022). Tuning the magnetic properties of $NiPS_3$ through organic-ion intercalation. *Nanoscale* 14, 1165–1173. doi:10.1039/D1NR07281A

Vaclavkova, D., Delhomme, A., Faugeras, C., Potemski, M., Bogucki, A., Suffczyński, J., et al. (2020). Magnetoelastic interaction in the two-dimensional magnetic material $MnPS_3$ studied by first principles calculations and Raman experiments. *2D Mater.* 7, 035030. doi:10.1088/2053-1583/ab93e3

Wang, F., Shifa, T. A., Yu, P., He, P., Liu, Y., Wang, F., et al. (2018a). New Frontiers on van der Waals layered metal phosphorous trichalcogenides. *Adv. Funct. Mater.* 28, 1802151. doi:10.1002/adfm.201802151

Wang, Y., Ying, J., Zhou, Z., Sun, J., Wen, T., Zhou, Y., et al. (2018b). Emergent superconductivity in an iron-based honeycomb lattice initiated by pressure-driven spin-crossover. *Nat. Commun.* 9, 1914. doi:10.1038/s41467-018-04326-1

Wang, Y., Zhou, Z., Wen, T., Zhou, Y., Li, N., Han, F., et al. (2016). Pressure-driven cooperative spin-crossover, large-volume collapse, and semiconductor-to-metal transition in manganese(II) honeycomb lattices. *J. Am. Chem. Soc.* 138, 15751–15757. doi:10.1021/jacs.6b10225

Wiedenmann, A., Rossat-Mignod, J., Louisy, A., Brec, R., and Rouxel, J. (1981). Neutron diffraction study of the layered compounds $MnPSe_3$ and $FePSe_3$. *Solid State Commun.* 40, 1067–1072. doi:10.1016/0038-1098(81)90253-2

Wildes, A. R., Fåk, B., Hansen, U. B., Enderle, M., Stewart, J. R., Testa, L., et al. (2023). Spin wave spectra of single crystal $CoPS_3$. *Phys. Rev. B* 107, 054438. doi:10.1103/PhysRevB.107.054438

Wildes, A. R., Kennedy, S. J., and Hicks, T. J. (1994). True two-dimensional magnetic ordering in $MnPS_3$. *J. Phys. Condens. Matter* 6, L335–L341. doi:10.1088/0953-8984/6/24/002

Wildes, A. R., Okamoto, S., and Xiao, D. (2021). Search for nonreciprocal magnons in $MnPS_3$. *Phys. Rev. B* 103, 024424. doi:10.1103/PhysRevB.103.024424

Wildes, A. R., Simonet, V., Ressouche, E., Ballou, R., and McIntyre, G. J. (2017). The magnetic properties and structure of the quasi-two-dimensional antiferromagnet $CoPS_3$. *J. Phys. Condens. Matter* 29, 455801. doi:10.1088/1361-648X/aa8a43

Wildes, A. R., Simonet, V., Ressouche, E., McIntyre, G. J., Avdeev, M., Suard, E., et al. (2015). Magnetic structure of the quasi-two-dimensional antiferromagnet $NiPS_3$. *Phys. Rev. B* 92, 224408. doi:10.1103/PhysRevB.92.224408

Yamaguchi, S., Okimoto, Y., Taniguchi, H., and Tokura, Y. (1996). Spin-state transition and high-spin polarons in $LaCoO_3$. *Phys. Rev. B* 53, R2926–R2929. doi:10.1103/PhysRevB.53.R2926

Yan, Y., Feng, D., Zhu, J., Zhou, Q., Tian, F., Li, F., et al. (2023). Lattice and electronic structural evolutions in compressed multilayer $MnPS_3$. *J. Phys. Chem. C* 127, 17186–17193. doi:10.1021/acs.jpcc.3c03501

Zhang, Q., Hwangbo, K., Wang, C., Jiang, Q., Chu, J.-H., Wen, H., et al. (2021). Observation of giant optical linear dichroism in a zigzag antiferromagnet $FePS_3$. *Nano Lett.* 21, 6938–6945. doi:10.1021/acs.nanolett.1c02188

Zhang, X., Xu, Y., Halloran, T., Zhong, R., Broholm, C., Cava, R. J., et al. (2023). A magnetic continuum in the cobalt-based honeycomb magnet $BaCo_2(AsO_4)_2$. *Nat. Mater.* 22, 58–63. doi:10.1038/s41563-022-01403-1

Zheng, Y., Jiang, X.-x., Xue, X.-x., Dai, J., and Feng, Y. (2019). *Ab initio* study of pressure-driven phase transition in $FePS_3$ and $FePSe_3$. *Phys. Rev. B* 100, 174102. doi:10.1103/PhysRevB.100.174102

Zobel, C., Kriener, M., Bruns, D., Baier, J., Grüninger, M., Lorenz, T., et al. (2002). Evidence for a low-spin to intermediate-spin state transition in $LaCoO_3$. *Phys. Rev. B* 66, 020402. doi:10.1103/PhysRevB.66.020402